Accounting for modeling errors in linear inversion of crosshole ground-penetrating radar amplitude data: detecting sand in clayey till

Badsberg Jensen Bolette[1], Hansen Thomas Mejer[2], Nielsen Lars[1], Cordua Knud Skou[3], Tuxen Nina[4], Tsitonaki Aikaterini[5], and Looms Majken Caroline[1]

[1]Department of Geosciences and Natural Resource Management, University of Copenhagen
[2]Aarhus University
[3]Department of Geosciences and Natural Resource Management
[4]Capital Region of Denmark, Center for Regional Development
[5]WSP Denmark A/S

November 16, 2022

Abstract

Mapping high permeability sand occurrences in clayey till is fundamental for protecting the underlying drinking water resources. Crosshole ground penetrating radar (GPR) amplitude data have the potential to differentiate between sand and clay, and can provide 2D subsurface models with a decimeter-scale resolution. We develop a probabilistic straight-ray-based inversion scheme, where we account for the forward modeling error arising from choosing a straight-ray forward solver. The forward modeling error is described by a Gaussian probability distribution and included in the total noise model by addition of covariance models. Due to the linear formulation, we are able to decouple the inversion of traveltime and amplitude data and obtain results fast. We evaluate the approach through a synthetic study, where synthetic traveltime and amplitude data are inverted to obtain slowness and attenuation tomograms using several noise model scenarios. We find that accounting for the forward modeling error is fundamental to successfully obtain tomograms without artifacts. This is especially the case for inversion of amplitude data since the structure of the noise model for the forward modeling error is significantly different from the other data error models. Overall, inversion of field data confirms the results from the synthetic study; however, amplitude inversion performs slightly better than traveltime inversion. We are able to characterize a 0.4 - 0.6 m thick sand layer as well as internal variations in the clayey till matching observed geological information from borehole logs and excavation.

Accounting for modeling errors in linear inversion of crosshole ground-penetrating radar amplitude data: detecting sand in clayey till

B. B. Jensen[1,3*], T. M. Hansen[2], L. Nielsen[1], K. S. Cordua[1], N. Tuxen[3], A. Tsitonaki[4], M. C. Looms[1]

[1]University of Copenhagen, Øster Voldgade 10, 1350 Copenhagen K

[2]Aarhus University, Høegh-Guldbergs Gade 2, 8000 Aarhus C

[3]Capital Region of Denmark, Kongens Vænge 2B, 3400 Hillerød

[4]WSP Denmark A/S, Linnés Allé 2, 2630 Taastrup

Key Points:

- Crosshole GPR amplitude field data is inverted using a probabilistic linear inversion scheme
- The forward modeling error is accounted for by estimating and including a Gaussian probability distribution
- Attenuation tomograms can be obtained successfully given that forward modeling errors are accounted for

*Funded by Innovation Fund DK

Corresponding author: Bolette Badsberg Jensen, `bbj@ign.ku.dk`

Abstract

Mapping high permeability sand occurrences in clayey till is fundamental for protecting the underlying drinking water resources. Crosshole ground penetrating radar (GPR) amplitude data have the potential to differentiate between sand and clay, and can provide 2D subsurface models with a decimeter-scale resolution. We develop a probabilistic straight-ray-based inversion scheme, where we account for the forward modeling error arising from choosing a straight-ray forward solver. The forward modeling error is described by a Gaussian probability distribution and included in the total noise model by addition of covariance models. Due to the linear formulation, we are able to decouple the inversion of traveltime and amplitude data and obtain results fast. We evaluate the approach through a synthetic study, where synthetic traveltime and amplitude data are inverted to obtain slowness and attenuation tomograms using several noise model scenarios. We find that accounting for the forward modeling error is fundamental to successfully obtain tomograms without artifacts. This is especially the case for inversion of amplitude data since the structure of the noise model for the forward modeling error is significantly different from the other data error models. Overall, inversion of field data confirms the results from the synthetic study; however, amplitude inversion performs slightly better than traveltime inversion. We are able to characterize a 0.4 - 0.6 m thick sand layer as well as internal variations in the clayey till matching observed geological information from borehole logs and excavation.

Plain Language Summary

Sand structures embedded in low permeable clayey till act as highways for water and contaminant transport. Detailed knowledge about these sand structures is important for estimation of how water and contamination moves down to the underlying drinking water reservoirs. Crosshole ground penetrating radar (GPR) can differentiate between sand and clay due to the contrast in electrical material properties and obtain 2D geological models of the subsurface between boreholes. We develop a simple linear approach

for geophysical inversion of the recorded amplitude data. A linear model can introduce errors in the estimated subsurface models. We account for this modeling error by including a Gaussian description of the error in the inversion. We find that accounting for the modeling error is fundamental to successfully obtain 2D subsurface models from inversion of amplitude data. We are able to characterize a 0.4 - 0.6 m thick sand layer as well as internal variations in the clayey till matching observed geological information from borehole logs and excavation. The developed method is able to obtain subsurface models fast and allows for estimation of uncertainty of the obtained solution.

1 Introduction

Heterogeneous glacial sediments, such as clayey till, dominate large parts of the near-surface geology of the Northern Hemisphere (Houmark-Nielsen, 2010). Sand layers and lenses control water and contaminant flow pathways in the otherwise low-permeable clay matrix. Delineation and characterization of these sand structures and bodies are necessary to determine the timing, the amount and the quality of the water percolating through these sediments (e.g. Gravesen et al., 2014).

A method for mapping these sand occurrences is by using crosshole ground penetrating radar (GPR). GPR is a fast, minimally invasive, electromagnetic method, which provides information on subsurface electrical properties with a decimeter scale resolution between boreholes located up to 5-7 m apart. The electrical properties of the subsurface can be linked to parameters important for flow and transport processes, such as volumetric water content or porosity by petrophysical relations (e.g. Topp et al., 1980). GPR has consequently been used in numerous hydrogeological studies (e.g. Hubbard et al., 1997; Binley et al., 2001; Klotzsche et al., 2013; Z. Zhou et al., 2020). For a more detailed review of the crosshole GPR method and applications we refer to Annan (2005) and Klotzsche et al. (2018).

The electromagnetic (EM) wave propagation between a transmitter antenna and a receiver antenna is governed by the subsurface dielectric permittivity and electrical conductivity. GPR has mainly been applied in low-conductive materials, such as sand, due to the attenuation of the signal through the subsurface. However, Looms et al. (2018) showed that crosshole GPR can be applied in high-conductive clay-rich environments. They showed that coherent sand layers in a matrix of clayey till can be accurately characterized, i.e. defining their depth, thickness and tilt, through the use of crosshole GPR. The exact locations of the sand structures were more accurately delineated by the amplitude information (related to the electrical conductivity) than by the traveltime information (related to the dielectric permittivity) of the recorded EM wave. The changes in measured amplitude ranged over several orders of magnitude, while changes in traveltime were at best two-fold.

In order to obtain a tomographic image describing the 2D subsurface variation between boreholes, geophysical inversion of the GPR data must be performed. Variations in the EM wave velocity are mainly governed by the water content of the formation (e.g. Topp et al., 1980). This means that under saturated conditions, the traveltime data may fall short in distinguishing between sand and clay structures, if they have similar porosities. Instead, the attenuation field obtained from amplitude inversion are expected to provide a means for distinguishing between sand and clay under saturated conditions. This implies that there is a potential for using amplitude inversion to identify and characterize sand lenses in clayey till.

Amplitude inversion has historically not been extensively performed as traveltime inversion has been considered a simpler and more robust procedure. Within the last decade, full-waveform inversion (FWI) schemes have been developed using both traveltime and amplitude information of the waveform data and yielding simultaneous estimation of relative dielectrical permittivity and electrical conductivity at potentially high resolution. The steepest-descent based FWI scheme initially developed by J. Ernst et al. (2007) and subsequently improved by G. A. Meles et al. (2010) and Mozaffari et al. (2020), has been used extensively. Klotzsche et al. (2019) provides a comprehensive overview of the method and its applications. However, the method has its limitations. The algorithm depends on the ability to accurately model the physics involved in the EM wave propagation, such as diffraction, refraction, interference and coupling effects near the antenna. It is at present not standard procedure to model antennae explicitly and it is therefore necessary to estimate a source wavelet, which is typically assumed constant for a given survey. Furthermore, the method requires a starting model that fulfills that its forward response lies within half a period of the observed waveform data to enable global convergence of the algorithm (G. Meles et al., 2011). The resulting dielectrical permittivity and the electrical conductivity tomograms do not necessarily exhibit similar spatial structures (e.g. Keskinen et al., 2019; Klotzsche et al., 2019). The estimated structures in the dielectrical permittivity tomograms are considered more reliable and more in line with expected geology (Oberröhrmann et al., 2013; Klotzsche et al., 2013).

Finally, this FWI-scheme is a deterministic inversion, hence it provides one solution to the inverse problem, which does not allow for direct uncertainty estimates. Alternatively, probabilistic FWI schemes can be employed such as Hunziker et al. (2019) and Cordua et al. (2012) to obtain such statistical information about the solution. However, both the deterministic FWI-scheme and the probabilistic FWI methods are computationally expensive, and their complexity make them inaccessible for non-experts. These challenges push towards the wish of revisiting simpler linear inversion schemes that are fast, robust and provide uncertainty estimates of the obtained subsurface models.

Linearized amplitude inversion is considered more uncertain than traveltime tomography as it depends on pre-inversion estimation of radiation patterns, antenna source strength and geometric correction of the wavefield propagation (see e.g., Holliger et al. (2001), Maurer and Musil (2004), B. Zhou and Fullagar (2001)). Correspondingly, linear inversion of amplitude values has only been performed with limited success (e.g., Holliger et al. (2001), Holliger and Maurer (2004)), and the resulting tomograms have been contaminated with artifacts. Maurer and Musil (2004) were able to overcome some of these obstacles in amplitude inversion and showed that the attenuation tomograms were improved when accounting for a varying data error along the depth of the boreholes.

The linearization of the highly non-linear EM wave propagation problem requires a simplified description of the underlying physical processes. Choosing such an approximate model for the forward problem will give rise to modeling errors, which will, if their magnitude is significant compared to the measurement errors, introduce systematic errors in the solution space. In recent years, the importance of accounting for modeling errors when using approximate forward solvers has been acknowledged (Hansen et al., 2014; Linde et al., 2017; Hansen & Cordua, 2017; Köpke et al., 2018; Levy et al., 2021, etc.).

Several approaches to handle the modeling error have recently been developed. Fundamental for the methods is the ability to compute the discrepancy between data calculated from a more accurate forward solver as opposed to an approximate forward solver. Hansen et al. (2014) presented a general method for inferring a Gaussian parameterization of the modeling error which can be computed prior to the inversion and accounted for in the total noise model. The method has since been applied in Hansen and Cordua (2017). Other methods that do not imply a Gaussian modeling error have been developed, for example handling the modeling error by projecting the residual term to a constructed orthonormal basis for the modeling error. Köpke et al. (2018) accounted for the modeling error term during the inversion through occasional runs of the more-accurate forward solver, whereas Köpke et al. (2019) used principal component analysis on a number of modeling error realizations and constructed a general description prior to the inversion. Finally, Levy et al. (2021) used a neural network approach to handle the modeling error in a Monte Carlo Markov Chain (MCMC) based inversion of GPR traveltime.

In this study we present a fast and simple inversion approach, where first-arrival traveltime data and maximum first-cycle amplitude data are inverted using a linear least-squares (LSQ) solution with Gaussian a priori information. We apply the methodology proposed by Hansen et al. (2014) and develop the method further to allow for inversion of amplitude data. This is to the best of our knowledge, the first study where forward modeling errors are included in inversion of crosshole GPR amplitude data. We quantify and account for the forward modeling error arising from choosing a straight-ray forward solver as opposed to a finite-difference-time-domain (FDTD) 2D forward solver, and we demonstrate how accounting for this modeling error affects the obtained inversion results. First, a synthetic study that serves as a proof-of-concept is presented, followed by a field study. We choose to present inversion results of both traveltime and amplitude data for completeness and for the comparison of amplitude and traveltime inversion results. Moreover, we discuss the general implications and advantages linked to applying this approach for interpretation of crosshole GPR data.

2 Field site

The developed methodology will be applied to field data acquired at a field site located at the Kallerup gravel pit in Denmark, see Figure 1 for approximate location. The near-surface geological conditions in the area are characterized by glacial deposits. At the field site, a unit of clayey till is observed in the upper 10 m of the subsurface with a sand occurrence of 0.4 - 0.6 m thickness observed in borehole logs between 1.40 - 2.35 m depth, and a coherent sand layer observed below 6.11 - 6.75 m depth (Looms et al., 2018). A detailed description of the sand structures in the field site area can be found in Kessler et al. (2012).

Furthermore, the site was excavated after the crosshole GPR measurements (see Larsen et al. (2016) for further details). Data presented in this study were obtained between boreholes RT1 and RT3. Two interpreted transects, Transect B and Transect C,

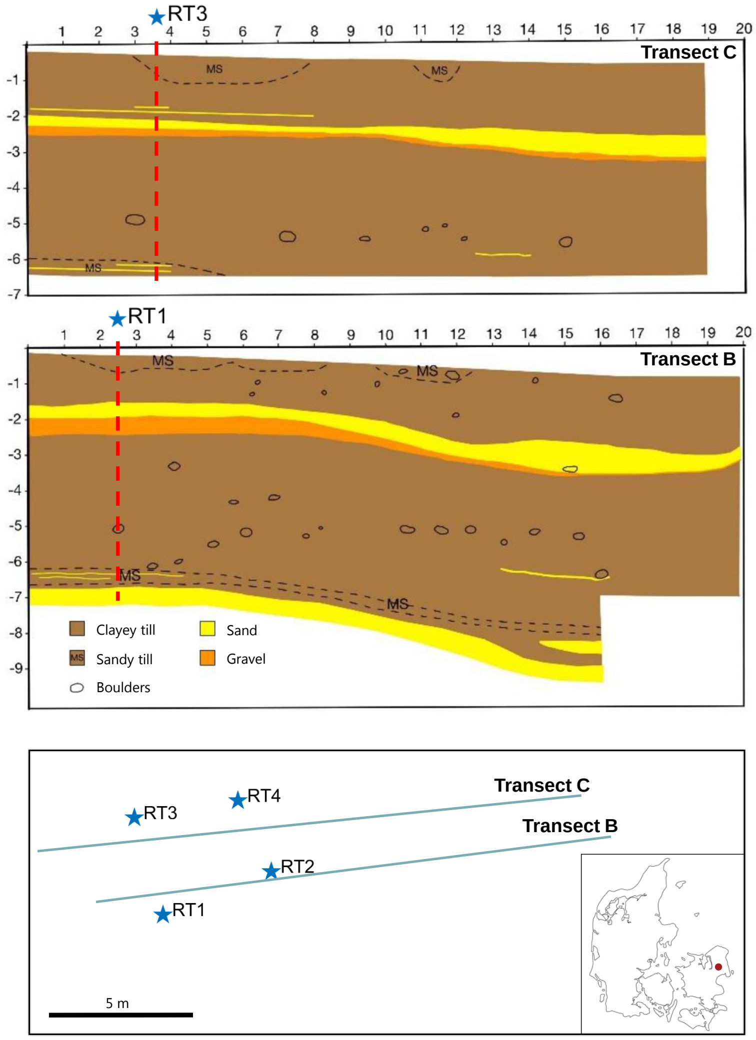

Figure 1. Upper and middle: Transect C and B with projected approximate borehole locations, modified from (Larsen et al., 2016). Lower: Map of field site location in Denmark, geological transects and borehole locations.

are seen in Figure 1, as well as their location relative to the boreholes (lowermost plot). The transects serve as a representative example of the geology at the field site. The locations of boreholes RT1 and RT3, are orthogonally projected onto the transects (upper and middle), but we would like to stress that this placement of the boreholes is approximate.

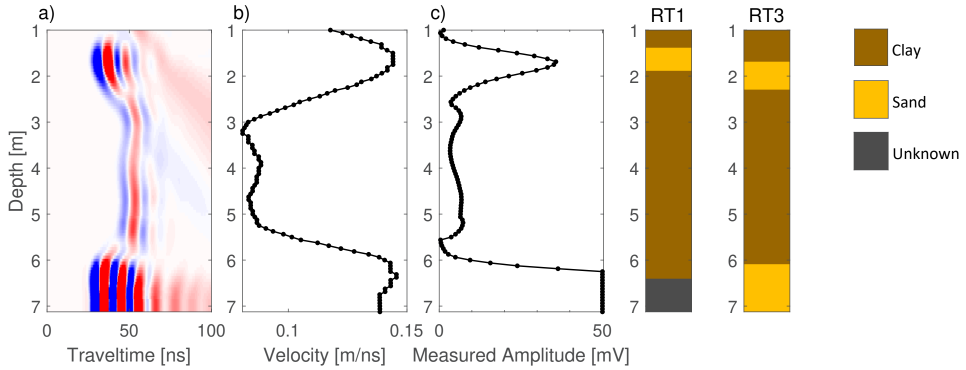

Figure 2. a) ZOP data from the transect RT1-RT3. b) Average velocity from first-arrival traveltime data and c) First-cycle maximum amplitude data. Borehole logs from borehole RT1 and RT3.

3 Crosshole GPR data

The crosshole GPR data were acquired using Sensors and Software's PulseEKKO system with 100 MHz antennae deployed in PEH tubes with a diameter of 0.063 m that were installed in the boreholes immediately after drilling. Calibration gathers in air were collected for absolute time zero correction of first-arrival traveltime data (Oberröhrmann et al., 2013). Zero-offset-profile (ZOP) data were collected in vertical increments of 12.5 cm, and shown in Figure 2 to illustrate the field data. We also show the corresponding average EM wave velocity obtained from picked first-arrival traveltime data, and first-cycle maximum amplitude data.

The Multi-offset-gather (MOG) dataset was collected by fixing the transmitter antenna at a given depth while lowering the receiver antenna in vertical increments of 0.25 m. The transmitter was then moved 0.25 m down and the procedure was repeated until the transmitter had covered the entire borehole depth intervals. The MOG data were collected from 1.0 to 7.0 m below top of PEH tubes. The transmitter antenna was in RT1 and the receiver antenna was in RT3 at all times. Sampling frequency was 0.4 ns, and the borehole distance was 3.37 m. High-angle traces with acquisition angles above 45 degrees from horizontal were discarded, similar to e.g. Linde et al. (2006); Looms et al. (2010). Traces significantly affected by the surface wave were also discarded, and the first us-able trace was obtained approximately 0.9 m below ground level. We obtain a MOG data set with 412 traces in total. For further information on the data set from Kallerup, see Looms et al. (2021) and Looms et al. (2018). First-arrival traveltime and maximum first-cycle amplitude data were manually picked from the obtained MOG waveform data set.

4 Methods

For both synthetic data and field data we apply straight-ray-based (i.e. linear) inversion scheme with Gaussian prior information. The important parts of the method applied in this study are presented in the following sections. The code was written in MatLab using the SIPPI toolbox developed by Hansen et al. (2013).

4.1 The inverse problem

In the geophysical forward problem, a given set of data $\vec{d}$ can be computed from a set of subsurface model parameters $\vec{m}$ by using the possibly nonlinear forward operator $g(\cdot)$

$$\vec{d} = g(\vec{m})\,. \tag{1}$$

The physics and the geometry of the forward problem is contained in $g(\cdot)$. The associated inverse problem consists of inferring information about the model parameters, $\vec{m}$, characterizing the subsurface from the observed data, $\vec{d}_{\mathrm{obs}}$.

In a probabilistic framework, the full solution to the inverse problem is formulated as a probability distribution, where states of information are combined to obtain the posterior distribution (Tarantola & Valette, 1982)

$$\sigma_M(\vec{m}) = k\rho_M(\vec{m})L(\vec{m})\,, \tag{2}$$

where k is a normalization factor, $\rho_M(\vec{m})$ describes the a priori information on the model parameters and the likelihood function, $L(\vec{m})$, is given by

$$L(\vec{m}) = \int d\vec{d} \frac{\rho_D(g(\vec{m}))\theta(\vec{d}|\vec{m})}{\mu_D(\vec{d})} \,. \tag{3}$$

The measurement uncertainties are described by $\rho_D(g(\vec{m}))$, and $\theta(\vec{d}|\vec{m})$ contains the information about the possibly uncertain forward relation (Tarantola & Valette, 1982). This can be given as $\theta(\vec{d}|\vec{m}) = \Lambda(\vec{d} - g(\vec{m}))$, where $d = g(\vec{m})$ is the forward relation, and the probability distribution $\Lambda(\vec{d}|\vec{m})$ is the modeling error that describes the uncertainty related to this forward relation. We refer to Hansen et al. (2014) for further details on $\Lambda(\vec{d}|\vec{m})$.

The solution to the linear inverse problem, $\vec{d} = \mathbf{G}\vec{m}$, with Gaussian measurement and modeling errors is then fully described by a Gaussian posterior probability distribution, $\sigma_M(\vec{m})$, characterized by the mean $\tilde{\vec{m}}$, and model covariance matrix, $\tilde{\mathbf{C}}_M$ (e.g. Tarantola, 2005, eq. 3.37)

$$\begin{aligned} \tilde{\vec{m}} &= \vec{m}_0 + \mathbf{C}_M \mathbf{G}' \left(\mathbf{G} \mathbf{C}_M \mathbf{G}' + \mathbf{C}_D \right)^{-1} \left(\vec{d}_{\mathrm{obs}} - \vec{d}_D - \mathbf{G}\vec{m}_0 \right) \\ \tilde{\mathbf{C}}_M &= \mathbf{C}_M - \mathbf{C}_M \mathbf{G}' \left(\mathbf{G} \mathbf{C}_M \mathbf{G}' + \mathbf{C}_D \right)^{-1} \mathbf{G} \mathbf{C}_M \,. \end{aligned} \tag{4}$$

A priori information on the model parameters describing the expected subsurface variation is incorporated through a Gaussian prior model, $\mathcal{N}(\vec{m}_0, \mathbf{C}_M)$. The observed data are given by $\vec{d}_{\mathrm{obs}}$, and the associated measurement and modeling errors are given by the data covariance matrix, $\mathbf{C}_D$. The linear kernel, $\mathbf{G}$, maps the model parameters to the observed data. Note that the bias correction, $\vec{d}_D$, is introduced according to Hansen et al. (2014). This general description of linear inversion can be used in inversion of various geophysical data. Here we apply the formulation to inversion of crosshole GPR traveltime and amplitude data.

4.2 Traveltime and amplitude tomography

The traveltime, t, is related to the slowness distribution, s, through the line integral for the ray path approximation of the signal sensitivty (e.g. Giroux et al., 2007; Peterson, 2001)

$$t = \int_0^r s(l) dl \, . \tag{5}$$

If velocity contrasts are small, ray-paths are approximately straight, and this expression can be linearized. From measurements of traveltime, t, the slowness distribution can be inferred by solving the inverse problem, $\vec{d} = \mathbf{G}\vec{m}$. The forward operator, $\mathbf{G}$, contains the ray-paths lengths. We choose to estimate the slowness distribution (inverse velocity) rather than the velocity distribution itself to keep the problem linear.

The measured amplitude is an exponential decay of the initial source amplitude, proportional to the attenuation, α, along the ray path through the subsurface (Giroux et al., 2007). Under the straight-ray assumption, the recorded amplitude can in 3D be estimated as (e.g. Holliger et al., 2001; Giroux et al., 2007):

$$A_m = A_0 \exp\left(-\alpha r\right) \Theta_{Tx} \Theta_{Rx} \frac{1}{L} \, . \tag{6}$$

This equation is only valid for a homogeneous medium and in the far-field regime (B. Zhou & Fullagar, 2001; Maurer & Musil, 2004). Prior to inversion, the measured amplitude, A_m, must be corrected according to equation 6. Corrections include: (1) The radiation patterns of the transmitter and receiver $\Theta_{Tx}\Theta_{Rx}$, which is approximated with radiation patterns for an electric dipole: $\Theta_{Tx}\Theta_{Rx} \approx \cos^2(\phi)$, where ϕ is the ray-path angle to horizontal. (2) The geometrical spreading of the energy. In 3D the correction factor is $1/L$, whereas synthetic 2D data is corrected with $1/\sqrt{L}$ (Mozaffari et al., 2020); And (3) The antenna gain effect, A_0, which is a scaling factor that accounts for the transmitter strength (B. Zhou & Fullagar, 2001). A_0 is typically unknown, but we assume that it is constant for our survey, consistent with Holliger et al. (2001); B. Zhou and Fullagar (2001); Peterson (2001).

To obtain a linear relationship between the measured amplitude and the attenuation, α, we first rearrange the terms and take the natural logarithm on both sides

$$-\ln\left(\frac{A_m L}{\Theta_{Rx}\Theta_{Tx}}\right) = \alpha r - \ln(A_0), \quad A_r = -\ln\left(\frac{A_m L}{\Theta_{Rx}\Theta_{Tx}}\right). \tag{7}$$

The antenna gain effect $-\ln(A_0)$ is then estimated by fitting a linear relation to the reduced amplitude A_r, against the ray-path length, following equation 7. The intersect at $r = 0$ is $-\ln(A_0)$. This is consistent with the approach suggested in B. Zhou and Fullagar (2001) and Peterson (2001). Subsurface heterogeneities introduce uncertainty on the estimate of A_0, and is observed by scatter around the fitted straight line. The correction and linearization of the amplitude data leads to a linear relation between subsurface attenuation and the log-linearized amplitude, τ

$$\tau = \alpha r = -\ln(A_m L) + \ln(\Theta_{Tx}\Theta_{Rx}) + \ln(A_0)\,. \tag{8}$$

This is formally comparable to the relation between traveltime and slowness and can be solved using the same linear inversion scheme, $\vec{d} = \mathbf{G}\vec{m}$, where $\mathbf{G}$ contains the same ray-paths lengths. For a further details on linearization and pre-inversion corrections of amplitude data, see Holliger et al. (2001), B. Zhou and Fullagar (2001) and Giroux et al. (2007).

4.3 Prior model setup (for forward simulation of waveform data)

We define a prior model which is setup to mimic the geological field site conditions. All synthetic waveform data are forward simulated in realizations from this prior. A spherical covariance model is chosen, to allow for a certain amount of subsurface roughness (Hansen et al., 2008), and horizontal and vertical correlation lengths are set to $h_{corr} =$

15 m and $v_{corr} = 1.5$ m, respectively. To obtain realizations that reflect the bimodal geology at Kallerup, we define target distributions for the relative dielectric permittivity, ε_r, and the electrical conductivity, σ. Each of the bimodal target distributions are constructed from two Gaussian distributions: one representative for the dominating clay component and one representative for the embedded sand structures. The mean parameter values are set to: $\varepsilon_{r,sand} = 5$, $\varepsilon_{r,clay} = 12.5$, for the relative electrical permittivity for sand and clay, respectively. For the electrical conductivity $\sigma_{sand} = 10$ mS/m and $\sigma_{clay} = 40$ mS/m. Realizations from the prior model are generated using the FFT-MA algorithm (Le Ravalec et al., 2000), which effectively generates unconditional realizations of a Gaussian random field. The Gaussian realizations are transformed by an inverse normal-score transformation (see e.g. Goovaerts et al., 2005) so the realizations honor the target distributions (Hansen et al., 2013). No correlation between ε_r and σ is assumed. The parameter values are defined independently, and realizations from the prior models are drawn independently.

The cell size for the bimodal prior models used in forward simulation of waveform data is dx = 0.03125 m = 32 cell/meter. The fine resolution is chosen to limit numerical dispersion of the forward solver used in the next step. The model area is defined from the outer limits of the transmitter and receiver positions.

Realizations from the bimodal prior models for ε_r and σ are transformed into realizations for attenuation, α, and slowness, s, using the high-frequency approximations (Annan, 2005)

$$s = \frac{\sqrt{\varepsilon_r}}{c}, \quad \alpha = \frac{\sigma}{2}\sqrt{\frac{\mu_0}{\varepsilon}}\,, \tag{9}$$

where c is the speed of light in vacuum, and μ_0 is free-space magnetic permeability. A sample from the bimodal prior model for both slowness and attenuation is seen in Figure 3.

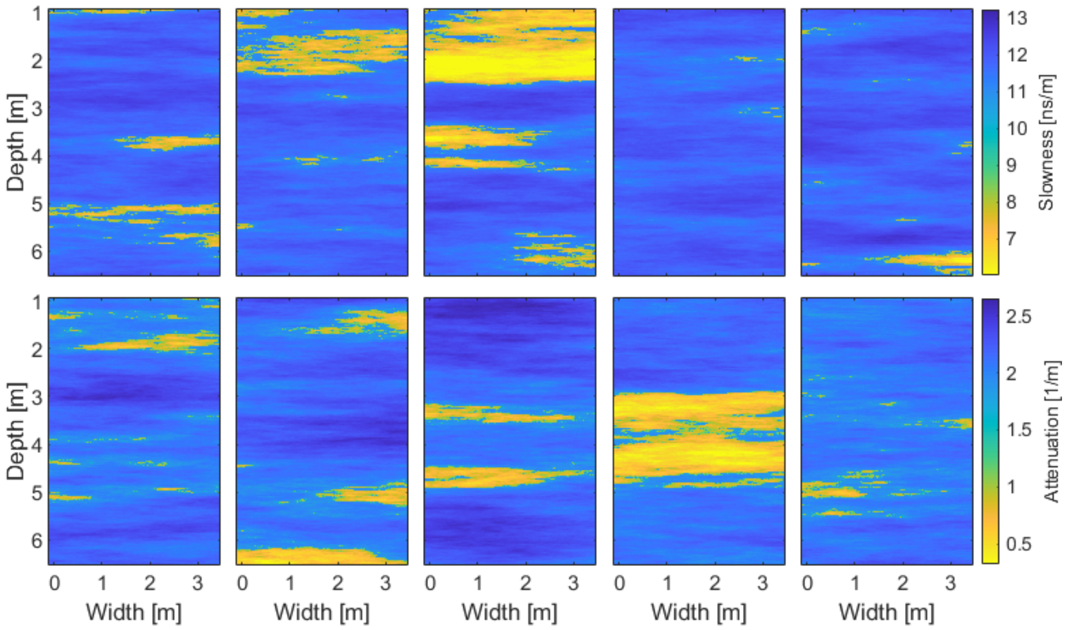

Figure 3. Five realizations from the bimodal prior distribution for slowness (upper row) and for attenuation (lower row).

4.4 Forward modeling

For realistic forward modeling of waveform data, we choose to employ a 2D finite-difference time-domain (FDTD) solution to Maxwell's equations (J. R. Ernst et al., 2006). The FDTD algorithm provides grid-based time-domain calculations of the EM wavefield propagation that yields second order accuracy in both time and space (J. Ernst et al., 2007). The edges of the defined model area are surrounded by a generalized perfectly matched layer (GPML), to avoid artificial reflections from the model edges (Ernst et al., 2007a; Fang and Wu, 1996).

4.5 Measurement and modeling errors

We consider three sources of errors, where each error source is described by a multivariate Gaussian distribution: (1) A forward modeling error arising from choosing a linear forward solver. This error is described by $\mathcal{N}(\vec{d}_T, \mathbf{C}_T)$. (2) Measurement errors that are described by $\mathcal{N}(\vec{d}_d, \mathbf{C}_d)$. (3) Other data errors arising from physical imperfections in the vicinity of the boreholes that not captured in our model parameterization. These errors are described by $\mathcal{N}(\vec{d}_p, \mathbf{C}_p)$.

The total noise model included in the linear inversion is obtained by treating all error sources as additive terms in the total data error covariance model and bias (Mosegaard & Tarantola, 2002; Hansen et al., 2014).

$$\vec{d}_D = \vec{d}_T + \vec{d}_d + \vec{d}_p, \quad \mathbf{C}_D = \mathbf{C}_T + \mathbf{C}_d + \mathbf{C}_p \,. \tag{10}$$

The individual Gaussian noise models are described below.

4.5.1 Forward modeling error

The forward modeling error is estimated by comparing approximate and 'exact' data from forward simulation of data in a number of realizations from the bimodal prior. Approximate traveltime and amplitude data are calculated using a straight-ray forward, and highly accurate data are obtained using a FDTD full waveform forward model, with subsequent picking of traveltime and amplitude data. In this way, a sample from the (unknown) probability distribution describing the forward modeling error, $\Lambda(\vec{d}|\vec{m})$, is obtained by subtracting the approximate data (straight-ray) $\mathbf{D}_{app}$ from the best data (full-waveform), $\mathbf{D}_{best}$

$$\mathbf{D}_\Lambda = \mathbf{D}_{best} - \mathbf{D}_{app} \,. \tag{11}$$

We use $N = 800$ realizations, since we experienced that above this number the obtained inversion tomograms did not change significantly. This is consistent with Hansen et al. (2014) who used $N = 600$ realizations as a basis for the model error characterization and Levy et al. (2021) who chose to use $N = 800$ samples.

If the modeling error is assumed Gaussian, $\mathcal{N}(\vec{d}_T, \mathbf{C}_T)$, the bias, $\vec{d}_T$, and the covariance, $\mathbf{C}_T$, can be estimated from the sample, $\mathbf{D}_\Lambda$ (Hansen et al., 2014) as

$$\begin{aligned} \vec{d}_T &= \left[d_T^1, d_T^2, ..., d_T^N\right] \\ \text{where} \quad d_T^i &= \frac{1}{N}\sum_{i=1}^{N}(D_{best}^{i,j} - D_{app}^{i,j}) \\ \mathbf{C}_T &= \frac{1}{N}\mathbf{D}_{\text{diff}}\mathbf{D}'_{\text{diff}} \\ \text{where} \quad \mathbf{D}_{\text{diff}} &= [\mathbf{D}_\Lambda - \mathbf{D}_T] \\ \text{and} \quad \mathbf{D}_T &= \left[\vec{d}_T, \vec{d}_T, ..., \vec{d}_T\right] . \end{aligned} \tag{12}$$

The inferred Gaussian description of the modeling error, $\mathcal{N}(\vec{d}_T, \mathbf{C}_T)$ is then incorporated in the linear inverse problem according to equation 10. We are aware that the modeling error is not necessarily strictly Gaussian, however, we describe the part of the modeling error that can be described by a Gaussian distribution. The same inferred Gaussian description of the forward modeling error is applied in both in the synthetic study and in the field data study, since the model error estimation only depends on: 1) The prior model, 2) Antenna geometry, 3) Choice of approximate and best forward model. If these are constant, the same inferred modeling error can be applied to multiple data sets.

4.5.2 Measurement errors

The measurement uncertainty is estimated to $\sigma_d = 0.4$ ns for traveltime and $\sigma_d = 0.12$ for the log-linearized amplitude data. The measurement uncertainty on amplitude data is estimated from analysis of repeated horizontal traces arising from acquiring both a ZOP and a MOG data set. The measurement uncertainty is described by the noise model $\mathcal{N}(\vec{d}_d, \mathbf{C}_d)$, where $\vec{d}_d = 0$ and $\mathbf{C}_d = \sigma_d^2 I$.

4.5.3 Imperfection data errors

Other sources of errors are also expected to be present in crosshole GPR data, as investigated by Cordua et al. (2008, 2009) and Peterson (2001). We account for data errors arising from unknown cavities in the borehole walls and small-scale anomalies close to the antenna positions following the approach presented in Cordua et al. (2008). These physical imperfections are not captured in our model parameterization and they are expected to cause correlated data errors. The correlated data error covariance for transmitter and receiver positions are estimated from $\mathbf{C}_{Tx}(i,j) = \mathbf{C}_{Rx}(i,j) = \sigma_p^2 \exp(-s(i,j)/L)$. The distance between the i'th and the j'th transmitter or receiver position is denoted $s(i,j)$ and L is the spatial correlation length. The data errors arising from the physical imperfections are described by the total data error covariance matrix calculated as $\mathbf{C}_p = \mathbf{C}_{Tx} + \mathbf{C}_{Rx}$, yielding the noise model $\mathcal{N}(\vec{d}_p, \mathbf{C}_p)$. These imperfection data errors are accounted for by addition of covariance matrices in the inversion, in a similar way as the forward modeling error. For traveltime, the standard deviation is chosen to be $\sigma_p = 0.8$ ns and the correlation length is set to L=5 m. The error parameterization is chosen based on values from a similar crosshole GPR survey using the same equipment (Cordua et al., 2008). The standard deviation in the calculation of the correlated error covariance is for the amplitude data chosen to be twice the measurement uncertainty, $\sigma_p = 0.24$, similar to the traveltime error parameterization. This is a first approximation as correlated data errors in amplitude data have not yet been investigated thoroughly. Correspondingly, the correlation length is set to L=5 m.

4.6 Prior information in LSQ inversion

A bimodal prior model is used for estimating the forward modeling error and for simulating synthetic waveform data, however, only Gaussian prior information can be included in the linear LSQ formulation of the solution to the inverse problem in equation 4. The mean and variance of the Gaussian prior for slowness and attenuation are approximated from the total mean and variance of the bimodal target distributions. The

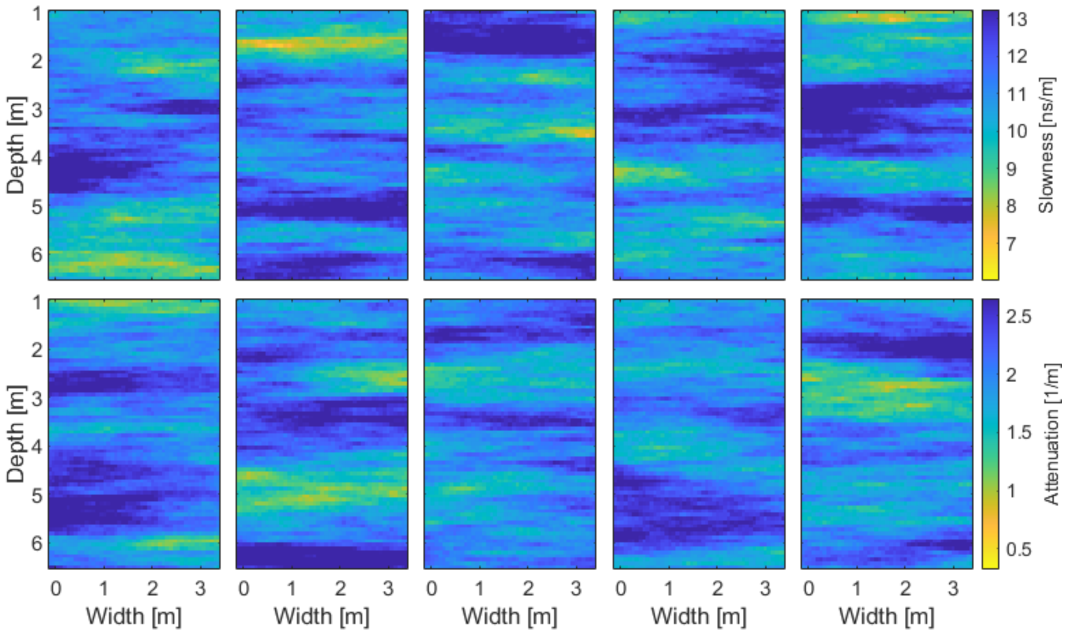

Figure 4. Five realizations from the Gaussian used in the linear inversion. For slowness (upper row) and attenuation (lower row).

covariance models are defined as for the bimodal prior, with the same parameter values: A spherical covariance model and correlation lengths of $h_{corr} = 15$ m, $v_{corr} = 1.5$ m. A sample from the Gaussian prior is seen in Figure 4.

4.7 Synthetic data

A synthetic data set is computed in one selected reference model which is a realization from the bimodal prior model. This reference model serves as ground truth for the synthetic study. The reference model is selected so it resembles some of the prominent geological features observed at the Kallerup field site.

Synthetic waveform data are simulated using the FDTD forward solver, followed by re-sampling to field data sampling frequency of $F_s = 0.4$ ns. Zero-mean white noise is added to the waveform data to obtain a reference data set. The root-mean-square of the noise is scaled to the mean amplitude value to ensure the same noise level on all traces, as often seen in field data. The used source wavelet was estimated in Looms et al. (2018), as part of a FWI of the data from Kallerup.

Synthetic traveltime data were picked automatically by using a cross-correlation based picking routine (Hansen et al., 2013; Molyneux & Schmitt, 1999). Maximum first cycle amplitudes were picked by automated picking of first peak above a defined threshold and above a minimum peak prominence. The amplitude data were corrected for antenna gain effects A_0, radiation patterns and geometrical spreading in 2D, as described above.

4.8 Field data pre-inversion processing

The traveltime field data acquired were corrected for absolute time zero (ATZ). The correction was obtained from interpolation of ATZs of several calibration gathers. Maximum first-cycle amplitude field data were linearized and corrected for geometric spreading in 3D, radiation patterns and antenna gain effects A_0 prior to inversion, in the same manner as the synthetic data set.

4.9 Inversion - accounting for modeling errors

Traveltime and log-linearized amplitude field data and syntetic data, are inverted using equation 4. The inversion resolution is set to dx=0.125 m. To investigate the influence of accounting for the forward modeling error, the inversion is performed accounting for several scenarios for the total noise model $\mathcal{N}(\vec{d}_D, \mathbf{C}_D)$:

(a) inversion using only measurement noise $\mathbf{C}_D = \mathbf{C}_d = \sigma^2\mathbf{I}$ and $\vec{d}_D = 0$.

(b) inversion using measurement noise and imperfection data errors $\mathbf{C}_D = \mathbf{C}_d + \mathbf{C}_p$ and $\vec{d}_D = 0$.

(c) inversion using only forward modeling errors $\mathbf{C}_D = \mathbf{C}_T$, and $\vec{d}_D = \vec{d}_T$.

(d) inversion using measurement noise and forward modeling errors $\mathbf{C}_D = \mathbf{C}_d + \mathbf{C}_T$ and $\vec{d}_D = \vec{d}_T$.

(e) inversion using measurement noise, imperfection data errors and forward modeling errors $\mathbf{C}_D = \mathbf{C}_d + \mathbf{C}_p + \mathbf{C}_T$, and $\vec{d}_D = \vec{d}_T$.

(f) inversion using only the bias correction $\vec{d}_D = \vec{d}_T$ of the forward modeling errors, measurement and imperfection data errors $\mathbf{C}_D = \mathbf{C}_d + \mathbf{C}_p$.

(g) inversion using only the forward modeling error covariance model $\mathbf{C}_D = \mathbf{C}_d + \mathbf{C}_p + \mathbf{C}_T$ but without the bias correction $\vec{d}_D = 0$.

The scenarios (f) and (g) were included to test the importance of the bias correction as opposed to the covariance model of the forward modeling error. The results from scenarios (f) and (g) are not presented here. In summary, the results showed that the ability to obtain meaningful tomograms are governed by the covariance model rather than the bias correction of the inferred forward modeling error description.

5 Results

5.1 Imperfection data errors and forward modeling errors

5.1.1 Impact of forward model choice

In Figure 5 (a) and (b), we present a random realization from the prior model for the relative dielectric permittivity, ε_r, and the electric conductivity σ, respectively. The corresponding forward estimated traveltime and log-linearized amplitude data are presented in Figure 5 (c) and (d). The approximate forward solver is a straight ray model, and the best forward solver is a 2D FDTD full waveform model as described earlier.

The full-waveform forward solver generally yields faster traveltimes compared to the straight ray forward. The fastest traveltimes are not necessarily associated with the shortest transmitter-receiver distance, since the scattered areas of lower permittivity values just above 3 m allow for a faster propagation velocity. This is seen in the full-waveform data and in the straight-ray data, however, the first arriving energy of the waveform data has not traveled along a straight path, giving rise to a large forward model error. The computed log-linearized amplitude data values (τ) are here generally lower when computed with the full waveform forward. The amplitude data show lower τ values at depths

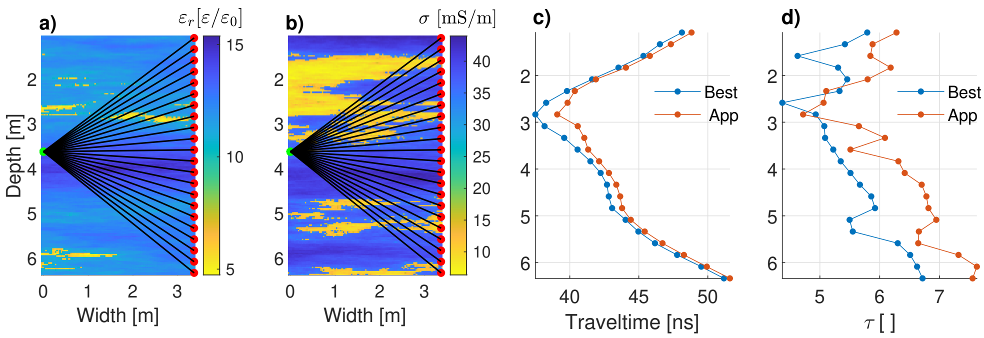

Figure 5. a) and b) A random realization from the bimodal prior model describing permittivity and conductivity, respectively. Difference in forward response computed with the approximate forward solver (straight ray) and best forward solver (full waveform). c) Traveltime and d) log-linearized amplitude.

with lower conductivity values, but the variations seem a bit shifted vertically, most prominent at 5.5 m depth. The τ values depend both on the waveform path but also on the conductivities. These effects may counteract each other, making it difficult to predict the resulting effect. This is particularly true in the investigated case, where we have chosen to decouple the prior models for ε_r and σ. The computed full waveform forward response can be both lower and higher than the computed straight-ray response for a given transmitter-receiver position. The latter is seen in Figure 5 (d) at approximately 2.3 and 2.9 m depth. The significant difference in data obtained from the chosen best forward (full waveform) and the approximate forward (straight ray) shows how important it is to account for this forward modeling error.

5.1.2 Modeling error sample

A sample of the forward modeling error was obtained from the bimodal prior model, as described in equation 11. The difference in the forward responses computed with the best and approximate forward solver, respectively, is presented in Figure 6.

The distribution for the traveltime modeling error is left skewed, whereas the distribution for the amplitude modeling errors is nearly symmetrical. Assuming Gaussian

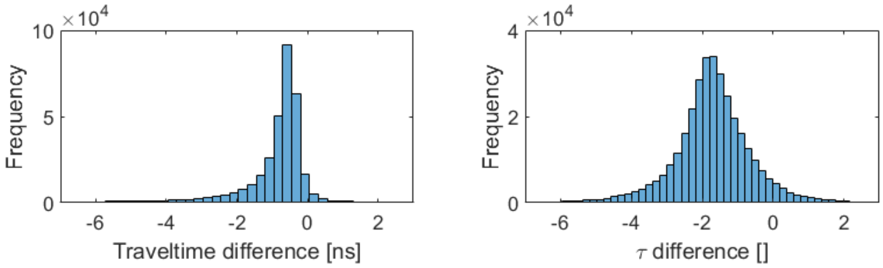

Figure 6. A sample, $\mathbf{D}_\Lambda = \mathbf{D}_{best} - \mathbf{D}_{app}$, of the forward modeling error computed in N=800 realizations from the bimodal prior model.

statistics, the mean traveltime forward modeling error is -0.98 ns with a standard deviation of 1.24 ns. The mean τ modeling error is -1.72 with a standard deviation of 1.11. The magnitude of these modeling errors for both traveltime and τ are several times larger than the estimated measurement uncertainties of 0.4 ns and 0.12, respectively.

5.1.3 Inferred Gaussian modeling error

From the sample of the forward modeling errors, a Gaussian model, $\mathcal{N}(\vec{d}_T, \mathbf{C}_T)$, is inferred for traveltime and log-linearized amplitude, τ, respectively. The inferred Gaussian covariance matrices, $\mathbf{C}_T$, for the forward modeling error for traveltime and log-linearized amplitude τ are seen in Figure 7 c) and 8 c), respectively. The assumed measurement noise is shown for comparison in Figure 7 a) and 8 a), while the calculated covariance matrices for the imperfection data errors $\mathbf{C}_p$ are shown in Figure 7 b) and 8 b). Finally, the total noise models used in the inversion of traveltime data and τ data are shown in Figure 7 d) and 8 d).

The off-diagonal elements of the inferred covariance matrices for both imperfections data errors and forward modeling errors, describe the spatial correlation between the individual data errors (Cordua et al., 2009). The off-diagonal covariances are significant, for both traveltime and τ data, indicating a strong spatial correlation as observed in Hansen et al. (2014) and Köpke et al. (2018). However, the spatial correlation properties for imperfections data errors and forward modeling errors are not the same.

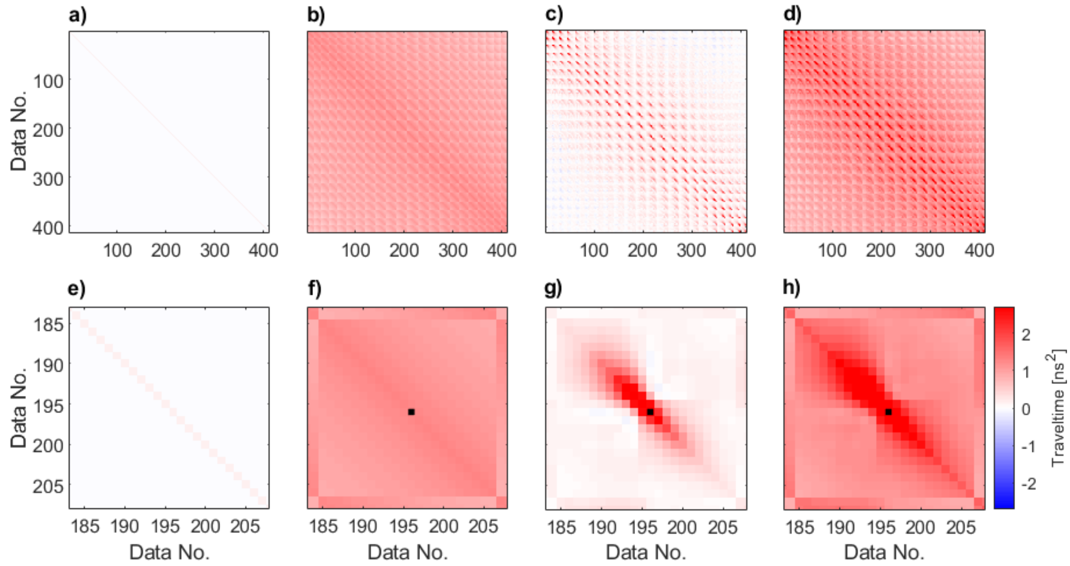

Figure 7. Traveltime error covariance. a) Measurement noise, $\mathbf{C}_d$, b) Imperfections data error covariance, $\mathbf{C}_p$, c) Forward modeling error covariance, $\mathbf{C}_T$, d) Total noise model, $\mathbf{C}_D = \mathbf{C}_d + \mathbf{C}_p + \mathbf{C}_T$. e)-h) zoomed view of the four covariance matrices, black dots indicate the receiver position closest to transmitter (angle ≈ 0).

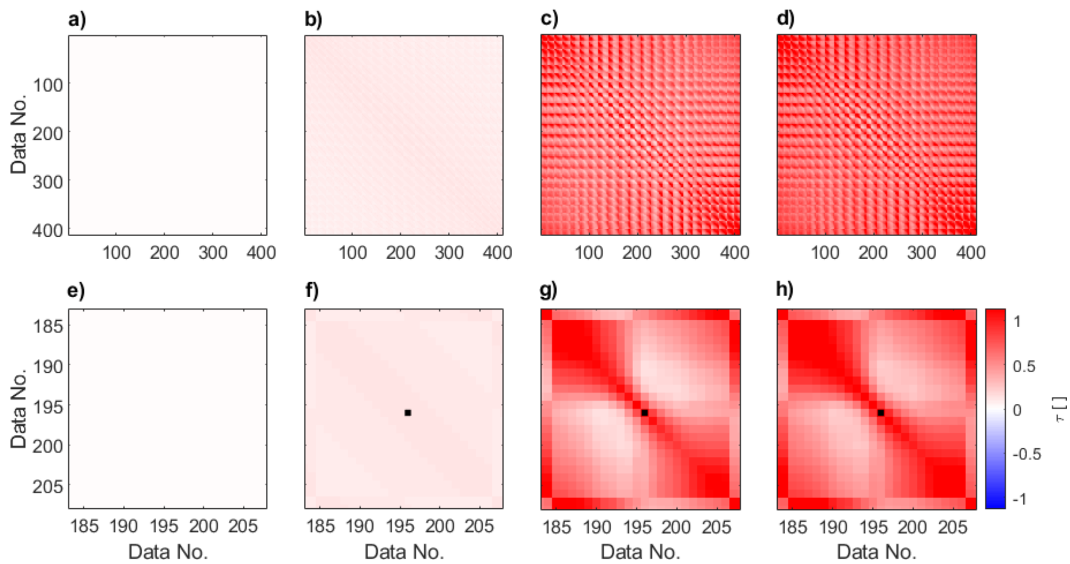

Figure 8. Log-linearized amplitude (τ) error covariance. a) Measurement noise, $\mathbf{C}_d$, b) Imperfections data error covariance, $\mathbf{C}_p$, c) Forward modeling error covariance, $\mathbf{C}_T$, d) Total noise model, $\mathbf{C}_D = \mathbf{C}_d + \mathbf{C}_p + \mathbf{C}_T$. e)-h) zoomed view of the four covariance matrices, black dots indicate the receiver position closest to transmitter (angle ≈ 0).

The blocky structure of the matrices arise from the acquisition configuration, where each block represents the data from one transmitter and the structure within each block describe the correlation between errors related to the receiver positions in the given gather. In the traveltime forward modeling error covariance matrix, Figure 7 c), it can be seen that data located close to each other exhibit a high model error covariance, and those far from each other have a close to zero or slightly negative error covariance. This is consistent with the results in Hansen et al. (2014). Conversely, for the log-linearized amplitude forward modeling error covariance, the correlation length is longer, and distant data points exhibit high error covariance.

To further investigate the spatial correlation between receiver positions in one gather, a zoomed view of the covariance matrices is shown in Figure 7 e-h) and 8 e-h). The black dot represents the receiver position closest to the transmitter (i.e. with the shortest ray-path). The highest amplitude error covariance is observed in the corners of the block, close to the diagonal, which represents receiver positions with high-angle ray-paths. Off-diagonals represent the error covariance between receiver positions further away. The error generally decreases with distance from a given position, but the error correlation seems to rebound for distant data locations.

The inferred bias correction, $\vec{d_T}$, computed from equation 12, represents the mean forward modeling error in each transmitter/receiver position. The bias correction for traveltime and log-linearized amplitude, τ, is shown in Figure 9 and Figure 10, respectively. The traveltime bias has a prominent angular dependence, with the highest bias associated with near-horizontal traces. Hence, the largest bias coincides with the direction of dominating correlation length in the prior model. For the log-linearized amplitude data, the bias also depends on the ray-path angle, but the highest biases are associated with higher angle rays.

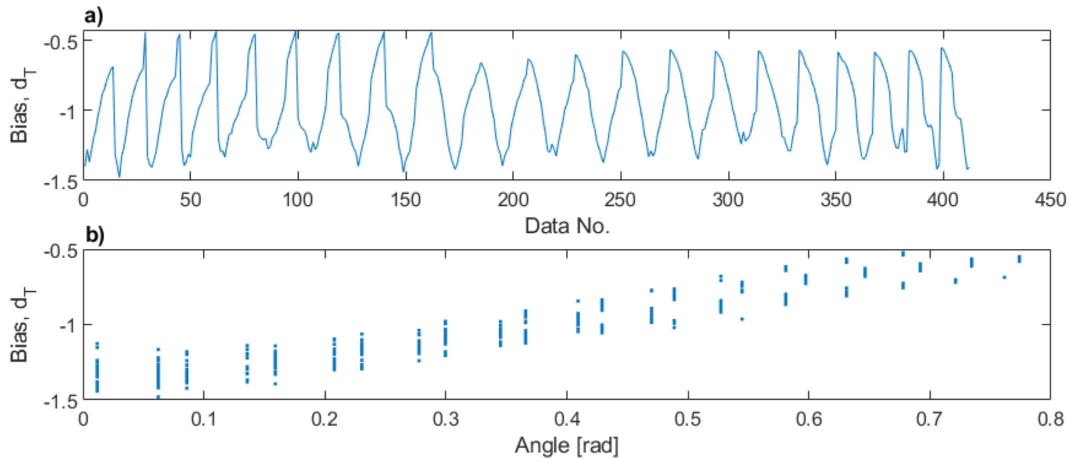

Figure 9. The inferred bias correction of the forward modeling error for traveltime. The bias correction is shown as a function of a) Data number and b) ray-path angle from horizontal.

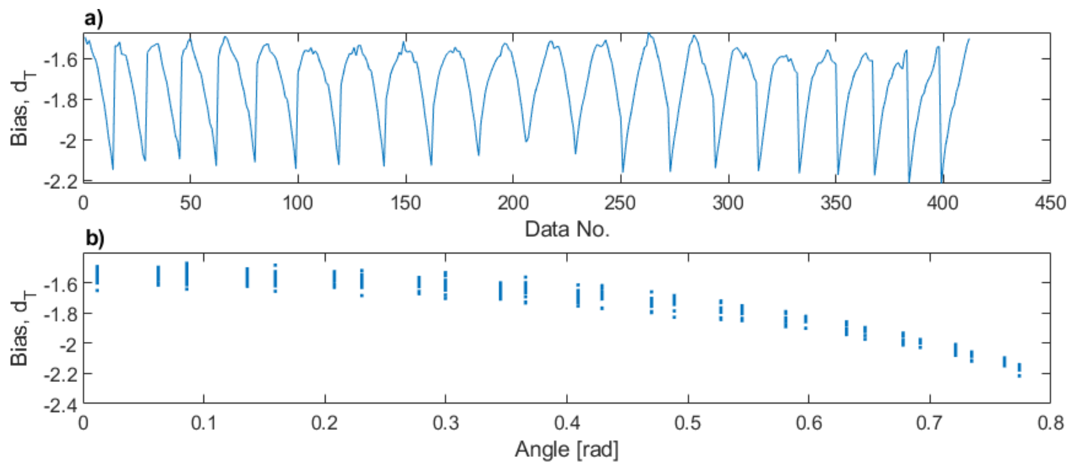

Figure 10. The inferred bias correction of the forward modeling error for log-linearized amplitude (τ). The bias correction is shown as a function of a) Data number and b) ray-path angle from horizontal.

5.2 Inversion results

In the following section, slowness and attenuation tomograms are presented. The data (both synthetic data and field data) were inverted accounting for several noise model scenarios as described earlier.

5.2.1 Synthetic data

The slowness tomograms obtained from inversion of synthetic traveltime data are seen in Figure 11. The attenuation tomograms obtained from inversion of synthetic log-linearized amplitude data, τ, are seen in Figure 12.

The reference models used as basis for simulating the synthetic data are displayed in the leftmost subplots, 5 realizations from the posterior distribution are displayed in subplots 1) - 5) and the LSQ estimates, i.e. the mean models, are presented with its corresponding uncertainty. The standard deviation is obtained from the diagonal of the estimated posterior model covariance $\tilde{\mathbf{C}}_M$.

For both the slowness and attenuation tomograms in Figure 11 (a) and Figure 12 (a), it is evident that when only measurement errors are accounted for, all tomograms are severely contaminated by artifacts. Features seem well-resolved, as they appear in all realizations, but the structures are not consistent with the reference models.

When imperfections data errors are included in the inversion (Figure 11 (b) and Figure 12 (b)), the artifacts are diminished, however still present, and the lateral structures are smeared. When the forward modeling errors are accounted for (Figure 11 (c), (d), (e) and Figure 12 (c), (d), (e)), the structures present in the tomograms become consistent with the reference models, and the coherence of the larger-scale lateral structures is recovered. The small high-attenuation structure at 6 m depth in Figure 12 (e), extending from x=0 m to x=2 m with a thickness of 15 - 20 cm, can be identified in some of the attenuation realizations, although it is not well resolved.

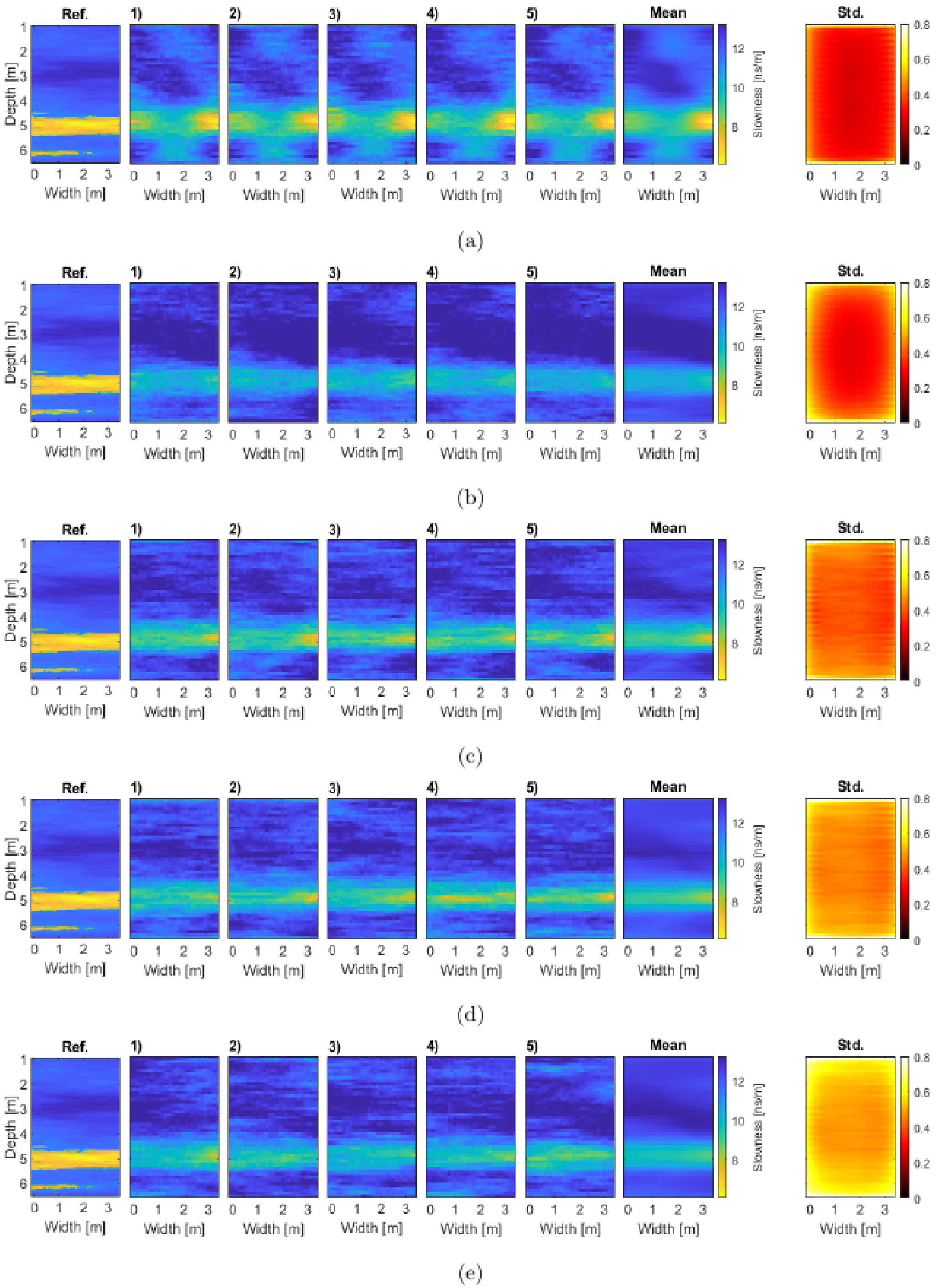

Figure 11. Slowness tomograms. Synthetic data. Reference model, 5 realizations from the posterior distribution, the LSQ estimate and its associated standard deviation. The total noise model used in the inversion is: (a) Measurement uncertainty accounted for, $\mathbf{C}_D = \sigma^2\mathbf{I}$ (b) Measurement uncertainty + imperfections data errors accounted for. $\mathbf{C}_D = \sigma^2\mathbf{I} + \mathbf{C}_p$. (c) Only forward modeling errors accounted for. $\mathbf{C}_D = \mathbf{C}_T$. (d) Measurement uncertainty + modeling errors accounted for. $\mathbf{C}_D = \sigma^2\mathbf{I} + \mathbf{C}_T$. (e) Measurement uncertainty + imperfections data errors + forward modeling errors accounted for. $\mathbf{C}_D = \sigma^2\mathbf{I} + \mathbf{C}_p + \mathbf{C}_T$.

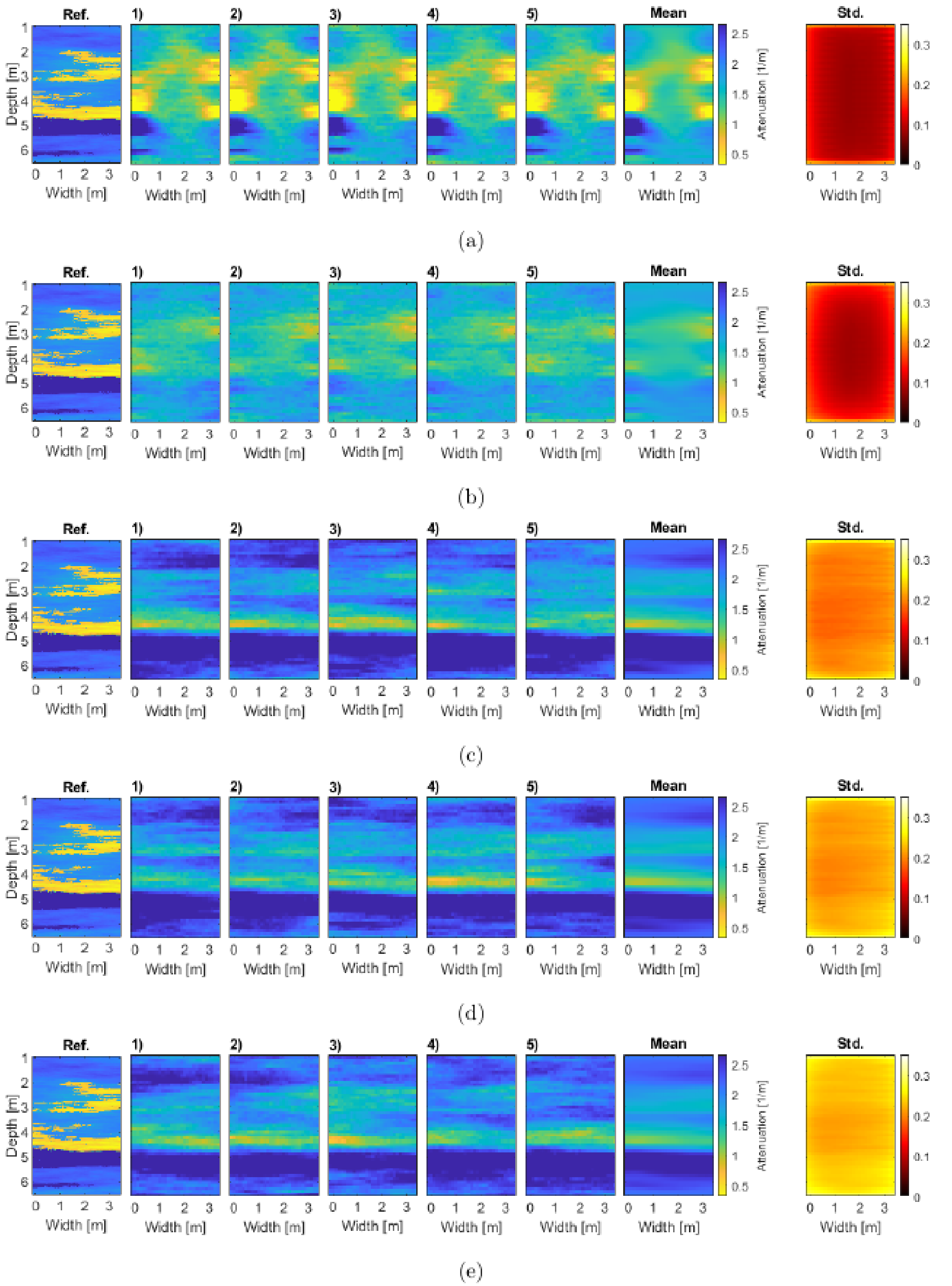

Figure 12. Attenuation tomograms. Synthetic data. Reference model, 5 realizations from the posterior distribution, the LSQ estimate and its associated standard deviation. The total noise model used in the inversion is: (a) Measurement uncertainty accounted for, $\mathbf{C}_D = \sigma^2\mathbf{I}$ (b) Measurement uncertainty + imperfections data errors accounted for. $\mathbf{C}_D = \sigma^2\mathbf{I} + \mathbf{C}_p$. (c) Only forward modeling errors accounted for. $\mathbf{C}_D = \mathbf{C}_T$. (d) Measurement uncertainty + modeling errors accounted for. $\mathbf{C}_D = \sigma^2\mathbf{I} + \mathbf{C}_T$. (e) Measurement uncertainty + imperfections data errors + forward modeling errors accounted for. $\mathbf{C}_D = \sigma^2\mathbf{I} + \mathbf{C}_p + \mathbf{C}_T$.

In general, the range of the parameter values for attenuation and slowness are not recovered in the LSQ estimates, since a LSQ solution will produces smooth results. This is also observed in the realizations as they are drawn from a Gaussian posterior distribution and not the correct bimodal distribution, i.e. compare realizations in Figure 3 with Figure 11 and 12.

5.2.2 Field data

The methodology used for inversion of synthetic data is also applied to the field data from Kallerup. Figure 13 and 14 show the results from inversion of traveltime and log-linearized amplitude data, respectively. Interpreted borehole logs from boreholes RT1 and RT3, are shown for comparison.

Overall, we obtain similar results when inverting field data as in the synthetic study, as we see that accounting for the forward modeling errors greatly improve the ability to obtain tomograms with geologically reasonable structures.

In the traveltime inversion results in Figure 13 (b), apparently well-resolved features show up in a checkerboard pattern in both the LSQ estimate and the realizations from the posterior distribution. The artifacts are still present when both forward modeling errors and imperfection data errors are accounted for as seen in Figure 13 (e). The estimated slowness of the sand layer is approximately 6.4 ns/m in the LSQ estimate, which corresponds to a radar velocity of 0.16 m/ns. Overall, it is seen that the contrast between the high and low slowness structures is higher in the field inversion results than for the synthetic results.

In the amplitude inversion results in Figure 13 (a) and (b), low-attenuation features show up above and below the expected sand layer at 1.5 m depth. However, a coherent sand layer at 1.4 - 2.3 m depth is identified when accounting for the forward modeling errors (Figure 14(c), (d), (e)). Within the clayey till, a layer with lower attenuation values is observed at 3.5 - 5.5 m depth. This observation is consistent with the ge-

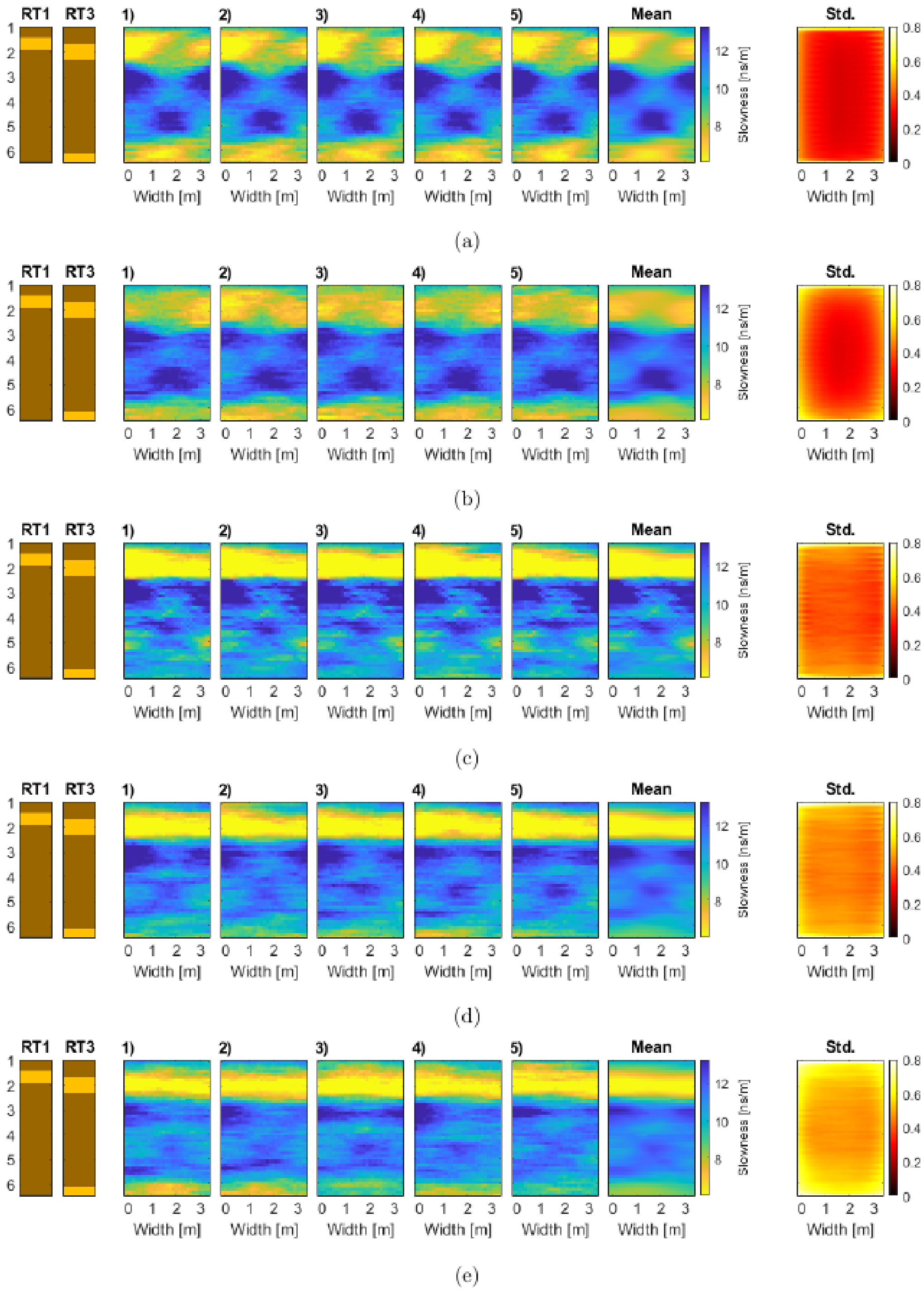

Figure 13. Slowness tomograms. Field data. Borehole logs, 5 realizations from the posterior distribution, the LSQ estimate and its associated standard deviation. The total noise model used in the inversion is: (a) Measurement uncertainty accounted for, $\mathbf{C}_D = \sigma^2\mathbf{I}$ (b) Measurement uncertainty + imperfections data errors accounted for. $\mathbf{C}_D = \sigma^2\mathbf{I} + \mathbf{C}_p$. (c) Only forward modeling errors accounted for. $\mathbf{C}_D = \mathbf{C}_T$. (d) Measurement uncertainty + modeling errors accounted for. $\mathbf{C}_D = \sigma^2\mathbf{I} + \mathbf{C}_T$. (e) Measurement uncertainty + imperfections data errors + forward modeling errors accounted for. $\mathbf{C}_D = \sigma^2\mathbf{I} + \mathbf{C}_p + \mathbf{C}_T$.

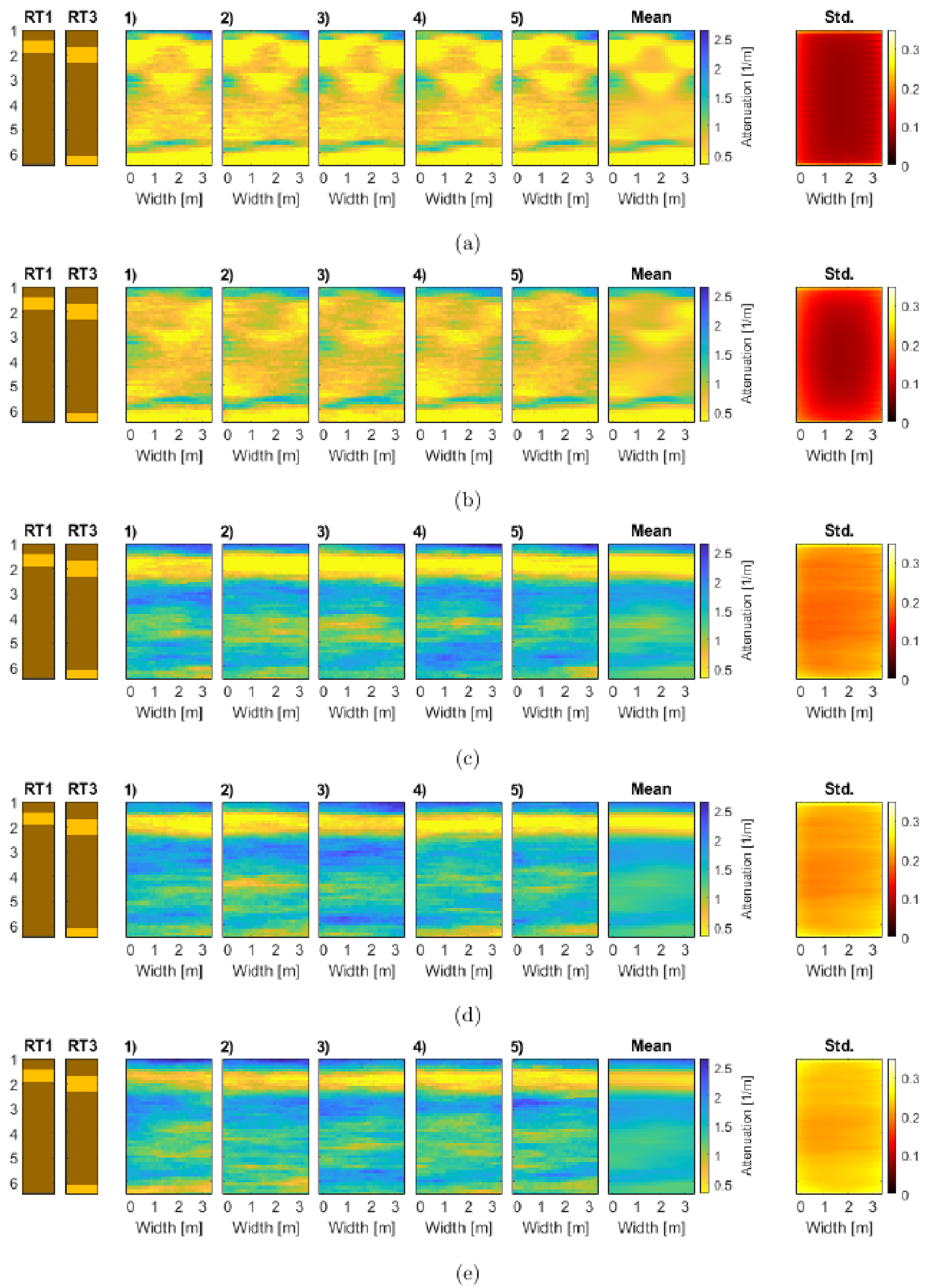

Figure 14. Attenuation tomograms. Field data. Borehole logs, 5 realizations from the posterior distribution, the LSQ estimate and its associated standard deviation. The total noise model used in the inversion is: (a) Measurement uncertainty accounted for, $\mathbf{C}_D = \sigma^2\mathbf{I}$ (b) Measurement uncertainty + imperfections data errors accounted for. $\mathbf{C}_D = \sigma^2\mathbf{I} + \mathbf{C}_p$. (c) Only forward modeling errors accounted for. $\mathbf{C}_D = \mathbf{C}_T$. (d) Measurement uncertainty + modeling errors accounted for. $\mathbf{C}_D = \sigma^2\mathbf{I} + \mathbf{C}_T$. (e) Measurement uncertainty + imperfections data errors + forward modeling errors accounted for. $\mathbf{C}_D = \sigma^2\mathbf{I} + \mathbf{C}_p + \mathbf{C}_T$.

ological description in Figure 1, where larger boulders and a more sandy till were identified at those depths.

The sand structure at ≈1.5 m depth is delineated narrower in the amplitude inversion results than in the traveltime inversion results. However, the Hedeland formation are better identified in the slowness tomograms than in the attenuation tomograms. Note that the last antenna position is 6.375 m in RT1 m and 6.335 m in RT3, which means there is only one source position located in the sand unit.

6 Discussion

The obtained tomograms from synthetic traveltime inversion in general show the same behavior as presented in Hansen et al. (2014). If the modeling error is not properly accounted for, well-resolved features are present in the estimated tomograms that are not part of the reference model. This is a consequence of mapping modeling errors into the posterior distribution. When accounting for the forward modeling error, the noise level increases but the features in the tomograms are consistent with the reference models.

For the linear inversion of synthetic and field amplitude data, we have shown that accounting for the modeling error is a crucial component in order to recreate the reference model or to obtain geologically reasonable attenuation tomograms, respectively. Numerous assumptions are violated in this strongly bimodal and heterogeneous subsurface, and yet we obtain successful results when accounting for the modeling error.

6.1 Forward modeling error

The magnitude of our estimated modeling error for traveltime is comparable to the results presented in Hansen et al. (2014) for similar subsurface prior models. Furthermore, the spatial structure of our inferred traveltime covariance model show the same tendencies as the previously published covariance matrices. Though Hansen et al. (2014)

used another data geometry than in this study, they also observed an angular dependency in the bias correction. We find, that the largest modeling error is associated with the direction of the dominant correlation length of the prior model, as also observed in Köpke et al. (2018). This direction coincides with the shortest ray-path length.

For the log-linearized amplitude case, we obtain a modeling error estimate of surprisingly high magnitude. The magnitude of the forward modeling error is comparable to the magnitude of the data itself and significantly larger than both the estimated measurement uncertainty and imperfections data errors. The structure of the inferred covariance matrix is different from what we see for traveltime. The spatial correlation lengths are longer and the covariance is positive for all transmitter-receiver positions. The modeling error itself is symmetric and yields both positive and negative values, as seen in Figure 6. This illustrates that the underlying physical processes that give rise to modeling errors in the amplitude data are more complex than for traveltime.

6.2 Tomograms

Solely accounting for imperfections data errors in the inversion of synthetic traveltime data, brings us far in terms of minimizing artifacts. However, from the prominent checkerboard artifacts in the slowness tomograms obtained from field data, it is evident that there are error sources that we do not successfully describe. Small uncertainties related to the borehole distances may cause this type of artifacts (Peterson, 2001), as well as the inclination of the boreholes that was not measured in this study. The ATZ corrections were estimated from measurements in air (Oberröhrmann et al., 2013), and these ATZ values may not be representative due to coupling effects associated with the material property of the clayey till formation as well as the heterogeneity along the borehole.

We observe prominent artifacts in the field attenuation tomograms near the upper and lower edges of the sand structure when modeling errors are not accounted for.

Holliger et al. (2001) and Holliger and Maurer (2004) observed similar artifacts near the edges of an anomaly. They attributed this type of artifacts to the diffractions associated with the edges of the anomaly and the inability of a ray-based inversion scheme to account for these diffractions. The inferred forward modeling error encompasses the statistics of these scattering and diffraction effects given a correct simulation of these effects in our best forward solver. This enables us to successfully obtain attenuation tomograms when the modeling error is accounted for.

Even though amplitude tomography is considered less robust than traveltime tomography due to the many approximations applied in the pre-inversion processing (Giroux et al., 2007), the field amplitude tomography in this study yields more convincing results than the field traveltime tomography. The sand layer at approximately 1.5 m depth is better delineated with amplitude data than with traveltime data. Furthermore internal variations in the clayey till unit are only apparent when inverting amplitude data. This may be due to the much larger range in amplitude data and the correspondingly larger contrast in the response from clay and sand. In Looms et al. (2018) this was accredited to the sensitivity of the amplitude data to even small amounts of clay and Holm-Jensen and Hansen (2020) observed a more narrow sensitivity kernel for the amplitude. This may also explain why the sand formation below 6 m depth is barely detected by amplitude data, while it is captured by traveltime data. The assertion about a more narrow sensitivity kernel for amplitude data is consistent with the ZOP data observed at the field site. The uncertainty related to borehole distance and inclination also affects amplitude data, furthermore one A_0 value was estimated before inversion of amplitude data. As for the ATZ correction, this assumption may be too crude in a heterogeneous environment, which may give rise to additional correlated data errors in amplitude data analogue to the uncertain ATZ correction. Finally, the correction for geometric attenuation is strictly only valid in a homogeneous medium (Peterson, 2001). Nonetheless, the magnitude of all these uncertainties may be insignificant relative to the prominent forward modeling error already accounted for in amplitude inversion.

6.3 Gaussian model description

We chose a Gaussian model to describe the forward modeling error. This allows us to account for the modeling error by simply adding the modeling error to the data errors. However, the subsurfaces studied here are bimodal with high velocity contrasts, and the Gaussian description of the forward modeling error may likely be inadequate. The incomplete noise model description may cause errors to be mapped into the solution space and introduce artifacts and this could be the main cause of the persistent artifacts in the field traveltime tomograms.

6.4 Practical aspects and perspectives

The computation time for estimating the forward model error based on $N = 800$ prior realizations was 8 hours on a standard workstation with 8 cores. The following linear inversion itself required only 1.5 seconds. The modeling error estimation can be carried out before field data acquisition, which enables obtaining field tomograms shortly after the field work has been conducted. The observed structure in the covariance models inferred for both traveltime and amplitude could indicate that analytical estimation of $\mathbf{C}_T$ and $\vec{d}_T$ is possible in similar way as the estimation of $\mathbf{C}_{corr}$ (Cordua et al., 2008), hence reducing computation time even further.

Even though there are advantages of a linear probabilistic method, we see a potential for improving the method further without sacrificing the simplicity in application. Our choice for the best forward model is a 2D FDTD full-waveform forward solver and hence some model discrepancy relative to the underlying process persists. The model discrepancy could be reduced by implementing a 3D forward solver as gprMax3D (Giannopoulos, 2005; Warren & Giannopoulos, 2017). The gprMax software is able to model the antennae explicitly, which would decrease the uncertainties related to varying coupling effects along the boreholes. Furthermore, gprMax is able to model the dispersive characteristics of clayey tills.

The structure of the modeling error covariance models could be improved by 3D forward simulation of data. However, the computational time required for inferring a 3D Gaussian model would increase significantly. Instead, the potentially increased magnitude of the 3D modeling error compared to 2D, could be quantified and used to correct the 2D forward modeling error parameterization. Out of plane effects could also be studied and possibly accounted for in a similar way.

7 Conclusion

We inverted crosshole GPR traveltime and amplitude data using a linear least-squares approach with included Gaussian a priori information. We accounted for the forward modeling errors arising from choosing a straight-ray forward model. Including the modeling error was fundamental in order to recover our synthetic reference model, but also to obtain geologically reasonable tomograms for field data. From the field data, we were able to delineate sand occurrences within a high-loss clayey till environment.

The estimated thickness and tilt of the upper sand layer correlate better to observations from borehole logs when inverting amplitude data rather than traveltime data. Furthermore, the attenuation tomograms exhibit internal variations within the clayey till that are in line with observations from the subsequent excavation and geological interpretation of the area.

In a complex subsurface as studied here, non-linear inversion schemes are expected to perform better. However, one important advantage of the linear formulation is that it enables independent inversion of amplitude and traveltime data, which is important for the use of crosshole GPR under fully saturated conditions. Furthermore, the probabilistic formulation allows for estimation of realistic measures of error of the inverse estimate.

Open Research

The traveltime and amplitude data used in the inversion in the study are available in (Looms et al., 2021) via https://doi.pangaea.de/10.1594/PANGAEA.934056. The source code for the SIPPI toolbox v1.6 used for simulation of prior models and waveform data can be downloaded from http://sippi.sourceforge.net/.

Acknowledgments

This work was funded by the Capital Region of Denmark and the Innovation Fund DK under the Industrial PhD Program, Grant #7091-00007B,

References

Annan, A. P. (2005). GPR Methods for Hydrogeological Studies. In *Hydrogeophysics* (pp. 185–213). Springer, Dordrecht. Retrieved from https://link.springer.com/chapter/10.1007/1-4020-3102-5_7 doi: 10.1007/1-4020-3102-5_7

Binley, A., Cassiani, G., Middleton, R., & Winship, P. (2001). Vadose zone flow model parametrisation using cross-borehole radar and resistivity imaging. *Journal of Hydrology*, *267*, 147–159. doi: 10.1016/S0022-1694(02)00146-4

Cordua, K. S., Hansen, T. M., & Mosegaard, K. (2012). Monte Carlo full-waveform inversion of crosshole GPR data using multiple-point geostatistical a priori information. *Geophysics*, *77*(2), H19–H31. Retrieved from http://library.seg.org/doi/10.1190/geo2011-0170.1 doi: 10.1190/geo2011-0170.1

Cordua, K. S., Looms, M. C., & Nielsen, L. (2008). Accounting for Correlated Data Errors during Inversion of Cross-Borehole Ground Penetrating Radar Data. *Vadose Zone Journal*, *7*(1), 263. Retrieved from https://www.soils.org/publications/vzj/abstracts/7/1/263 doi: 10.2136/vzj2007.0008

Cordua, K. S., Nielsen, L., Looms, M. C., Hansen, T. M., & Binley, A. (2009). Quantifying the influence of static-like errors in least-squares-based inversion and sequential simulation of cross-borehole ground penetrating radar data. *Journal of Applied Geophysics*, *68*(1), 71–84. Retrieved from http://dx.doi.org/10.1016/j.jappgeo.2008.12.002 doi: 10.1016/j.jappgeo.2008.12.002

Ernst, J., Maurer, H., Green, A., & Holliger, K. (2007, sep). Full-Waveform Inversion of Crosshole Radar Data Based on 2-D Finite-Difference Time-Domain Solutions of Maxwell's Equations. *IEEE Transactions on Geoscience and Remote Sensing*, *45*(9), 2807–2828. Retrieved from http://ieeexplore.ieee.org/document/4294093/ doi: 10.1109/TGRS.2007.901048

Ernst, J. R., Holliger, K., Maurer, H., & Green, A. G. (2006, feb). Realistic FDTD modelling of borehole georadar antenna radiation: Methodolgy and application. *Near Surface Geophysics*, *4*(1), 19–30. Retrieved from http://doi.wiley.com/10.3997/1873-0604.2005028 doi: 10.3997/1873-0604.2006004

Giannopoulos, A. (2005, dec). Modelling ground penetrating radar by GprMax. *Construction and Building Materials*, *19*(10), 755–762. doi: 10.1016/J.CONBUILDMAT.2005.06.007

Giroux, B., Gloaguen, E., & Chouteau, M. (2007). bh_tomo-a Matlab borehole georadar 2D tomography package. *Computers and Geosciences*, *33*(1), 126–137. doi: 10.1016/j.cageo.2006.05.014

Goovaerts, P., AvRuskin, G., Meliker, J., Slotnick, M., Jacquez, G., & Nriagu, J. (2005, jul). Geostatistical modeling of the spatial variability of arsenic in groundwater of southeast Michigan. *Water Resources Research*, *41*(7), 1–19. Retrieved from https://onlinelibrary.wiley.com/doi/full/10.1029/2004WR003705https://onlinelibrary.wiley.com/doi/abs/10.1029/2004WR003705https://agupubs.onlinelibrary.wiley.com/doi/10.1029/2004WR003705 doi: 10.1029/2004WR003705

Gravesen, P., Balling, I. M., Vignoli, G., Klint, K. E. S., Brüsch, W., Nilsson, B., … Rosenbom, A. E. (2014). Vurdering af mulighederne for udpegning af pesticidfølsomme lerområder (SFO-ler) på grundlag af eksisterende data. *GEUS for Naturstyrelsen*, *2*.

Hansen, T. M., & Cordua, K. S. (2017, dec). Efficient Monte Carlo sampling of inverse problems using a neural network-based forward-applied to GPR crosshole traveltime inversion. *Geophysical Journal International*, *211*(3), 1524–1533. Retrieved from http://academic.oup.com/gji/article/211/3/1524/4157792/Efficient-Monte-Carlo-sampling-of-inverse-problems doi: 10.1093/GJI/GGX380

Hansen, T. M., Cordua, K. S., Jacobsen, B. H., & Mosegaard, K. (2014). Accounting for imperfect forward modeling in geophysical inverse problems — Exemplified for crosshole tomography. *Geophysics*, *79*(3), H1–H21. Retrieved from http://library.seg.org/doi/10.1190/geo2013-0215.1 doi: 10.1190/geo2013-0215.1

Hansen, T. M., Cordua, K. S., Looms, M. C., & Mosegaard, K. (2013). SIPPI: A Matlab toolbox for sampling the solution to inverse problems with complex prior information: Part 1-Methodology. *Computers and Geosciences*, *52*, 470–480. Retrieved from http://dx.doi.org/10.1016/j.cageo.2012.09.004 doi: 10.1016/j.cageo.2012.09.004

Hansen, T. M., Looms, M. C., & Nielsen, L. (2008). Inferring the Subsurface Structural Covariance Model Using Cross-Borehole Ground Penetrating Radar Tomography. *Vadose Zone Journal*, *7*(1), 249. Retrieved from https://pubs.geoscienceworld.org/vzj/article-pdf/7/1/249/2997685/249.pdfhttps://www.soils.org/publications/vzj/abstracts/7/1/249 doi: 10.2136/vzj2006.0144

Holliger, K., & Maurer, H. (2004). Effects of stochastic heterogeneity on ray-based tomographic inversion of crosshole georadar amplitude data. *Journal of Applied Geophysics*, *56*(3), 177–193. doi: 10.1016/S0926-9851(04)00051-5

Holliger, K., Musil, M., & Maurer, H. R. (2001). Ray-based amplitude tomography for crosshole georadar data: a numerical assessment. *Journal of Applied Geophysics*, *47*, 285–298.

Holm-Jensen, T., & Hansen, T. M. (2020). Linear Waveform Tomography Inversion Using Machine Learning Algorithms. *Mathematical Geosciences*, *52*(1), 31–51. Retrieved from https://doi.org/10.1007/s11004-019-09815-7 doi: 10.1007/s11004-019-09815-7

Houmark-Nielsen, M. (2010, apr). Extent, age and dynamics of Marine Isotope Stage 3 glaciations in the southwestern Baltic Basin. *Boreas*, *39*(2), 343–359. Retrieved from http://doi.wiley.com/10.1111/j.1502-3885.2009.00136.x doi: 10.1111/j.1502-3885.2009.00136.x

Hubbard, S. S., Peterson, J. E., Roberts, J., & Wobber, F. (1997). Estimation of permeable pathways and water content using tomographic radar data. *The Leading Edge*, 1623–1628.

Hunziker, J., Laloy, E., & Linde, N. (2019). Bayesian full-waveform tomography with application to crosshole ground penetrating radar data. *Geophysical Journal International*, *218*(2), 913–931. Retrieved from `https://academic.oup.com/gji/article-abstract/218/2/913/5482080` doi: 10.1093/gji/ggz194

Keskinen, J., Looms, M. C., Klotzsche, A., & Nielsen, L. (2019). Practical Data Acquisition Strategy for Time-lapse Experiments Using Crosshole GPR and Full-Waveform Inversion. *Applied Geophysics*, *in prep*.

Kessler, T. C., Klint, K. E., Nilsson, B., & Bjerg, P. L. (2012, oct). Characterization of sand lenses embedded in tills. *Quaternary Science Reviews*, *53*(C), 55–71. Retrieved from `https://www.sciencedirect.com/science/article/pii/S0277379112003125http://dx.doi.org/10.1016/j.quascirev.2012.08.011` doi: 10.1016/j.quascirev.2012.08.011

Klotzsche, A., Jan van der Kruk, Niklas Linde, Joseph Doetsch, & Harry Vereecken. (2013). 3-D characterization of high-permeability zones in a gravel aquifer using 2-D crosshole GPR full-waveform inversion and waveguide detection. *Geophysical Journal International*, *195*(2), 932–944. doi: 10.1093/gji/ggt275

Klotzsche, A., Jonard, F., Looms, M., van der Kruk, J., & Huisman, J. (2018). Measuring Soil Water Content with Ground Penetrating Radar: A Decade of Progress. *Vadose Zone Journal*, *17*(1), 180052. Retrieved from `https://doi.org/10.2136/vzj2018.03.0052` doi: 10.2136/vzj2018.03.0052

Klotzsche, A., Vereecken, H., & Van Der Kruk, J. (2019, nov). Review of crosshole ground-penetrating radar full-waveform inversion of experimental data: Recent developments, challenges, and pitfalls. *Geophysics*, *84*(6), H13–H28.

Retrieved from http://library.seg.org/page/policies/terms doi: 10.1190/geo2018-0597.1

Köpke, C., Irving, J., & Elsheikh, A. H. (2018). Accounting for model error in Bayesian solutions to hydrogeophysical inverse problems using a local basis approach. *Advances in Water Resources*, *116*, 195–207. Retrieved from https://doi.org/10.1016/j.advwatres.2017.11.013 doi: 10.1016/j.advwatres.2017.11.013

Köpke, C., Irving, J., & Roubinet, D. (2019). Stochastic inversion for soil hydraulic parameters in the presence of model error: An example involving ground-penetrating radar monitoring of infiltration. *Journal of Hydrology*, *569*, 829–843. Retrieved from https://doi.org/10.1016/j.jhydrol.2018.12.016 doi: 10.1016/j.jhydrol.2018.12.016

Larsen, T. H. O., Palstrøm, P. O., & Larsen, L. O. (2016). *Kallerup Grusgrav: Kortlægning af sandlinser i moræneler* (Tech. Rep.). Orbicon A/S for Region Hovedstaden.

Le Ravalec, M., Noetinger, B., & Hu, L. Y. (2000). The FFT moving average (FFT-MA) generator: An efficient numerical method for generating and conditioning Gaussian simulations. *Mathematical Geology*, *32*(6), 701–723. Retrieved from https://link.springer.com/article/10.1023/A:1007542406333 doi: 10.1023/A:1007542406333

Levy, S., Hunziker, J., Laloy, E., Irving, J., & Linde, N. (2021, oct). Using deep generative neural networks to account for model errors in Markov chain Monte Carlo inversion. *Geophysical Journal International*, *228*(2), 1098–1118. Retrieved from https://academic.oup.com/gji/article/228/2/1098/6374556 doi: 10.1093/gji/ggab391

Linde, N., Binley, A., Tryggvason, A., Pedersen, L. B., & Revil, A. (2006, dec). Improved hydrogeophysical characterization using joint inversion of cross-hole electrical resistance and ground-penetrating radar traveltime data. *Water*

Resources Research, *42*(12). doi: 10.1029/2006WR005131

Linde, N., Ginsbourger, D., Irving, J., Nobile, F., & Doucet, A. (2017). On uncertainty quantification in hydrogeology and hydrogeophysics. *Advances in Water Resources*, *110*, 166–181. Retrieved from http://dx.doi.org/10.1016/j.advwatres.2017.10.014 doi: 10.1016/j.advwatres.2017.10.014

Looms, M. C., Hansen, T. M., Cordua, K. S., Nielsen, L., Jensen, K. H., & Binley, A. (2010). Geostatistical inference using crosshole ground-penetrating radar. *Geophysics*, *75*(6), J29–J41. Retrieved from http://library.seg.org/doi/10.1190/1.3496001https://doi.org/10.1190/1.3496001 doi: 10.1190/1.3496001

Looms, M. C., Klotzsche, A., van der Kruk, J., Larsen, T. H., Edsen, A., Tuxen, N., ... Nielsen, L. (2021). *Crosshole ground penetrating radar data collected in clayey till with sand occurrences* [data set]. PANGAEA. Retrieved from https://doi.org/10.1594/PANGAEA.934056 doi: 10.1594/PANGAEA.934056

Looms, M. C., Klotzsche, A., van der Kruk, J., Larsen, T. H., Edsen, A., Tuxen, N., ... Nielsen, L. (2018). Mapping sand layers in clayey till using crosshole ground-penetrating radar. *Geophysics*, *83*(1), A21–A26. Retrieved from https://library.seg.org/doi/10.1190/geo2017-0297.1 doi: 10.1190/GEO2017-0297.1

Maurer, H., & Musil, M. (2004, mar). Effects and removal of systematic errors in crosshole georadar attenuation tomography. *Journal of Applied Geophysics*, *55*(3-4), 261–270. Retrieved from https://www.sciencedirect.com/science/article/pii/S0926985104000059 doi: 10.1016/j.jappgeo.2004.02.003

Meles, G., Greenhalgh, S., van der Kruk, J., Green, A., & Maurer, H. (2011). Taming the non-linearity problem in GPR full-waveform inversion for high contrast media. *Journal of Applied Geophysics*, *73*(2), 174–186. Retrieved from `http://dx.doi.org/10.1016/j.jappgeo.2011.01.001` doi: 10.1016/j.jappgeo.2011.01.001

Meles, G. A., Van Der Kruk, J., Greenhalgh, S. A., Ernst, J. R., Maurer, H., & Green, A. G. (2010). A new vector waveform inversion algorithm for simultaneous updating of conductivity and permittivity parameters from combination crosshole/borehole-to- surface GPR data. *IEEE Transactions on Geoscience and Remote Sensing*, *48*(9), 3391–3407. doi: 10.1109/TGRS.2010.2046670

Molyneux, J. B., & Schmitt, D. R. (1999). First-break timing: Arrival onset times by direct correlation. *Geophysics*, *64*(5), 1492–1501. Retrieved from `http://geophysics.geoscienceworld.org/content/64/5/1492.abstract` doi: 10.1190/1.1444653

Mosegaard, K., & Tarantola, A. (2002). Probabilistic approach to inverse problems. In *International geophysics* (Vol. 81, pp. 237–265). Academic Press. doi: 10.1016/S0074-6142(02)80219-4

Mozaffari, A., Klotzsche, A., Warren, C., He, G., Giannopoulos, A., Vereecken, H., & van der Kruk, J. (2020, jun). 2.5D crosshole GPR full-waveform inversion with synthetic and measured data. *GEOPHYSICS*, *85*(4), H71–H82. Retrieved from `https://library.seg.org/doi/abs/10.1190/geo2019-0600.1` doi: 10.1190/geo2019-0600.1

Oberröhrmann, M., Klotzsche, A., Vereecken, H., & Van Der Kruk, J. (2013). Optimization of acquisition setup for cross-hole GPR full-waveform inversion using checkerboard analysis. *Near Surface Geophysics*, *11*(2), 197–209. doi: 10.3997/1873-0604.2012045

Peterson, J. E. (2001). Pre-inversion corrections and analysis of radar tomographic data. *Journal of Environmental and Engineering Geophysics*, *6*(1), 1–18. doi: 10.4133/JEEG6.1.1

Tarantola, A. (2005). *Inverse Problem Theory and Methods for Model Parameter Estimation*. Society for Industrial and Applied Mathematics. Retrieved from https://books.google.dk/books/about/Inverse_Problem_Theory_and_Methods_for_M.html?id=jKeHEWtzdKgC&redir_esc=yhttp://epubs.siam.org/doi/book/10.1137/1.9780898717921 doi: 10.1137/1.9780898717921

Tarantola, A., & Valette, B. (1982, may). Generalized nonlinear inverse problems solved using the least squares criterion. *Reviews of Geophysics*, *20*(2), 219–232. Retrieved from https://onlinelibrary.wiley.com/doi/full/10.1029/RG020i002p00219https://onlinelibrary.wiley.com/doi/abs/10.1029/RG020i002p00219https://agupubs.onlinelibrary.wiley.com/doi/10.1029/RG020i002p00219 doi: 10.1029/RG020i002p00219

Topp, G. C., Davis, J. L., & Annan, A. P. (1980). Electromagnetic Determination of Soil Water Content: Measruements in Coaxial Transmission Lines. *Water Resources Research*, *16*(3), 574–582. doi: 10.1029/WR016i003p00574

Warren, C., & Giannopoulos, A. (2017). Characterisation of a ground penetrating radar antenna in lossless homogeneous and lossy heterogeneous environments. *Signal Processing*, *132*. doi: 10.1016/j.sigpro.2016.04.010

Zhou, B., & Fullagar, P. K. (2001). Delineation of sulphide ore-zones by borehole radar tomography at Hellyer Mine, Australia. *Journal of Applied Geophysics*, *47*(3-4), 261–269. doi: 10.1016/S0926-9851(01)00070-2

Zhou, Z., Klotzsche, A., Hermans, T., Nguyen, F., Schmäck, J., Haruzi, P., … Van Der Kruk, J. (2020, nov). 3D aquifer characterization of the Hermalle-sous-Argenteau test site using crosshole ground-penetrating radar amplitude analysis and full-waveform inversion. *Geophysics*, *85*(6), H133–H148. Retrieved from http://library.seg.org/page/policies/terms doi: 10.1190/geo2020-0067.1